HHS Public Access

Author manuscript

Dev Cell. Author manuscript; available in PMC 2023 August 22.

Published in final edited form as:

Dev Cell. 2022 August 22; 57(16): 1976–1994.e8. doi:10.1016/j.devcel.2022.07.006.

N^6-Adenomethylation of *GsdmC* is essential for Lgr5$^+$ stem cell survival to maintain normal colonic epithelial morphogenesis

Jie Du[1,2], **Rajesh Sarkar**[1], **Yan Li**[3], **Lei He**[1], **Wenjun Kang**[3], **Wang Liao**[1,4], **Weicheng Liu**[1], **Tivoli Nguyen**[1], **Linda Zhang**[5], **Zifeng Deng**[1], **Urszula Dougherty**[1], **Sonia S. Kupfer**[1], **Mengjie Chen**[1,3], **Joel Pekow**[1], **Marc Bissonnette**[1], **Chuan He**[5,6], **Yan Chun Li**[1,7,*]

[1]Department of Medicine, Division of Biological Sciences, The University of Chicago, Chicago, Illinois, USA

[2]Department of Oral Medicine, School and Hospital of Stomatology, Shanxi Medical University, Taiyuan, Shanxi, China

[3]Center for Research Informatics, The University of Chicago, Chicago, Illinois, USA

[4]Department of Cardiology, Hainan General Hospital, Hainan Clinical Research Institute, Haikou, Hainan, China

[5]Departments of Chemistry, Biochemistry and Molecular Biology, The University of Chicago, Chicago, Illinois, USA

[6]Howard Hughes Medical Institute, The University of Chicago, Chicago, Illinois, USA

[7]Lead Contact

Summary

Gut epithelial morphogenesis is maintained by intestinal stem cells. Here we report that depletion of *N*^{6}-adenosine methyltransferase subunit Mettl14 from gut epithelial cells in mice impaired colon mucosal morphogenesis, leading to increased mucosal permeability, severe inflammation, growth retardation and premature death. *Mettl14* ablation triggered apoptosis that depleted Lgr5$^+$ stem cells and disrupted colonic organoid growth and differentiation, whereas inhibition of apoptosis rescued *Mettl14*-deleted mice and organoids. Mettl14 depletion disrupted *N*^{6}-adenomethylation on *GsdmC* transcripts and abolished GsdmC expression. Reconstitution of *Mettl14*-deleted organoids or mice with GSDMC rescued Lgr5 expression and prevented apoptosis and mouse premature death, whereas GSDMC silence eliminated LGR5 and triggered apoptosis

*Correspondence: Yan Chun Li, cyan@medicine.bsd.uchicago.edu.

Author contributions

Conceptualization: Y.C.L.; Methodology and Investigation: J.D., R.S., L.H., W.L.,T.N., L.Z; Formal analysis: Y.L., W.K., W.L., M.C., Y.C.L.; Writing – Original Draft: J.D., Y.L., L.H., Y.C.L.; Writing – Review & Editing: S.S.K., J.P., M.B., C.H., Y.C.L.; Fund Acquisition: C.H., Y.C.L.; Resources: L.Z., Z.D., U.D., S.S.K., J.P., M.B., C.H; Supervision: Y.C.L.

Declaration of interests

C.H. is a scientific founder and a member of the scientific advisory board of Accent Therapeutics, Inc. The other authors declare no competing interests.

in human colonic organoids and epithelial cells. Mechanistically, Mettl14 depletion eliminated mitochondrial GsdmC, disrupted mitochondrial membrane potential and triggered cytochrome c release that activates the pro-apoptotic pathway. In conclusion, *GsdmC* N^6-adenomethylation protects mitochondrial homeostasis and is essential for $Lgr5^+$ cell survival to maintain normal colonic epithelial regeneration.

eTOC Blurb

Gut mucosal epithelial homeostasis is maintained by intestinal stem cells. Du et al. demonstrate that N^6-adenomethylation of *GsdmC* mRNA is required for the survival of colonic $Lgr5^+$ intestinal stem cells so as to sustain normal colonic mucosal morphogenesis in mice.

Graphical Abstract

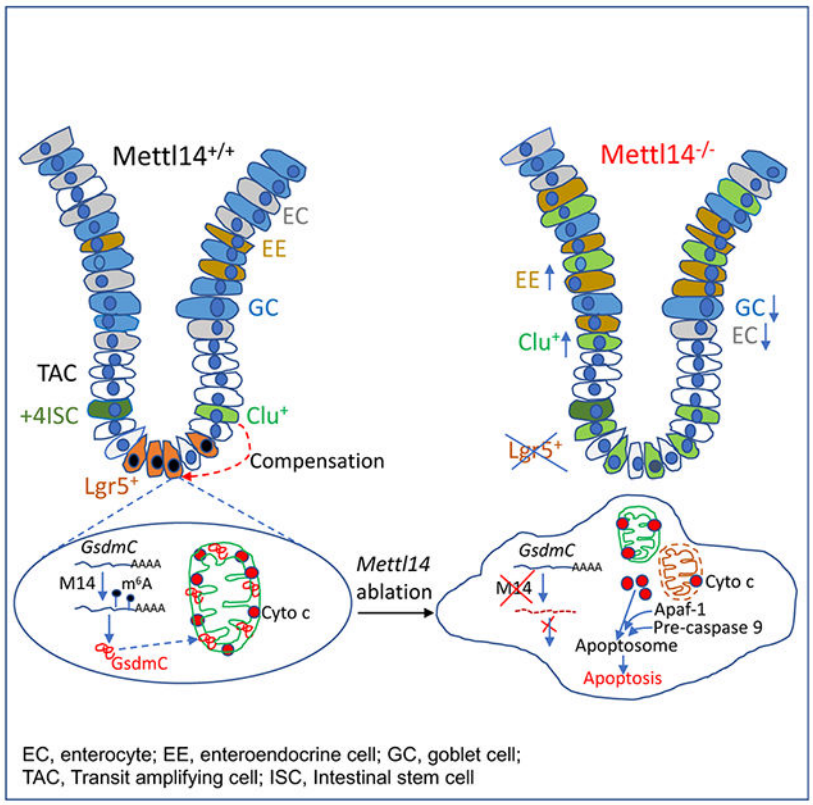

Introduction

The intestine is a sophisticated system that involves complex interplays among the intestinal mucosal barrier, immune system and microbiota. The mucosal barrier consists of a monolayer of epithelial cells and associated mucus that prevent luminal microorganisms, toxins and antigens from entering the body (Laukoetter, et al., 2006; Watson, et al., 2005). To balance the constant insults from the luminal environment, the epithelial layer undergoes continuous renewal, in which a diversity of differentiated cell types with distinct functions, namely absorptive enterocytes and secretory cells including goblet cells, enteroendocrine

cells, Paneth cells and tuft cells, are constantly regenerated (Noah, et al., 2011). This continuous epithelial regeneration is maintained by the intestinal stem cells (ISCs) located at the base of the crypt, which are responsible for replenishing the entire epithelium through cell division and differentiation (Perochon, et al., 2018; Noah and Shroyer, 2013). To a large extent intestinal homeostasis is maintained by ISC self-renewal and differentiation and a balance in proliferation, differentiation and death of precursor and differentiated cells.

N^6-adenomethylation (m^6A) of polyadenylated RNA transcripts is the most abundant internal post-transcriptional modification of eukaryotic RNAs, constituting ~0.4-0.6% of all adenosine nucleotides in mammalian RNAs (Frye, et al., 2018). RNA m^6A is reversible and dynamically regulated by writers, erasers and readers. Writers are methyl-transferases that install the methyl group, erasers are demethylases that remove the methyl group, and readers are proteins that recognize and interact with the m^6A site (Zaccara, et al., 2019). The m^6A methyl-transferase is a protein complex composed of multiple proteins including methyltransferase-like 3 (METTL3), METTL14 and Wilms tumor 1-associated protein (WTAP) (Liu, et al., 2014; Ping, et al., 2014). Two m^6A erasers have been identified: fat mass and obesity-associated protein (FTO) and ALKBH5 (Huang, et al., 2020; Zheng, et al., 2013; Jia, et al., 2011). The reader proteins include members of YT521-B homology (YTH) domain-containing proteins, heterogeneous nuclear ribonucleoprotein (HNRNP) proteins (Zhao, et al., 2017), and insulin-like growth factor 2 mRNA-binding proteins (Huang, et al., 2018). The readers mediate the function of m^6A (Shi, et al., 2018; Shi, et al., 2017; Du, et al., 2016; Alarcon, et al., 2015; Wang, et al., 2014a). It is now recognized that m^6A influences all fundamental aspects of mRNA metabolism, including mRNA processing, stability and translation (Zaccara, et al., 2019; Zhao, et al., 2017). Recent studies have unveiled broad physiological functions of m^6A, which range from determination of stem cell fate and pluripotency, regulation of immunity to learning and memory (Du, et al., 2020; Lee, et al., 2019; Koranda, et al., 2018; Shi, et al., 2018; Weng, et al., 2018; Cui, et al., 2017; Li, et al., 2017; Zhang, et al., 2017; Chen, et al., 2015; Geula, et al., 2015; Batista, et al., 2014; Wang, et al., 2014b). Although a few recent studies have begun to focus on intestinal m^6A (Han, et al., 2020), the role of m^6A in intestinal epithelial morphogenesis and regeneration remains largely unknown.

In this context, we sought to explore the role of epithelial m^6A in intestinal physiology by genetically targeting Mettl14, a core subunit of the m^6A methyltransferase. Our studies demonstrate that RNA m^6A plays a critical role in the regulation of intestinal homeostasis; particularly, we discovered that m^6A of gasdermin (Gsdm) C transcripts is essential for $Lgr5^+$ ISC survival to maintain normal colonic epithelial morphogenesis.

Results

Deletion of *Mettl14* from gut epithelial cells leads to severe growth retardation and premature death.

To study the role of m^6A methyltransferase in intestinal physiology, we crossed *Mettl14*$^{flox/flox}$ ($M14^{f/f}$) mice (Du, et al., 2020) and Villin-Cre mice to generate *Mettl14*$^{flox/flox}$;Villin-Cre (IEC-$M14^{-/-}$) mice. The *villin* promoter targets Cre expression to gut epithelial cells including small and large intestines (Madison, et al., 2002). As expected,

IEC-M14$^{-/-}$ mice showed deletion of Mettl14, but not Mettl3, in intestinal epithelial cells (Fig. S1A,B), causing >80% reduction in colonic epithelial m^{6}A (Fig. S1C). Although the offspring displayed a normal Mendelian distribution, IEC-M14$^{-/-}$ mice showed marked growth retardation in both males and females compared to their M14$^{f/f}$ counterparts and were ~40% smaller in body weight (Fig. 1A,B). The weight differences between M14$^{f/f}$ and IEC-M14$^{-/-}$ mice mainly occurred postnatally. Remarkably, >60% of IEC-M14$^{-/-}$ mice died before 10 weeks of age (Fig. 1C). IEC-M14$^{-/-}$ mice developed severe colitis, and had a very high disease activity index (Fig. 1D), which assesses the extent of body weight loss, diarrhea, bleeding and lethargy (Van der Sluis, et al., 2006), suggesting severe intestinal problems.

Epithelial Mettl14 depletion impaires colonic epithelial morphogenesis leading to spontaneous colitis and systemic inflammation.

Histological examination of the intestines revealed relatively normal small intestinal structures (not shown) but markedly disorganized colonic epithelial structure in young (<4wks old) IEC-M14$^{-/-}$ mice (Fig. S1D). IEC-M14$^{-/-}$ mice surviving >10 wks developed mucosal hyperplasia with extensive immune cell infiltration (Fig. 1E), reminiscent of chronic mucosal inflammation. Mucosal myeloperoxidase (MPO) activity, a marker of neutrophil infiltration, was substantially increased in IEC-M14$^{-/-}$ mice (Fig. 1F). Immunostaining confirmed an increase in CD3$^+$ and CD45$^+$ cell infiltration (Fig. S1E). As a result, IEC-M14$^{-/-}$ mice had very high histological scores, calculated based on the extent of immune cell infiltration, goblet cell depletion, mucosal thickening and architectural destruction (Rath, et al., 1996) (Fig. 1G). One remarkable defect in IEC-M14$^{-/-}$ colonic mucosa was a dramatic decrease in mature goblet cells, revealed by Alcian blue staining that specifically stains mucus, and confirmed by mucin 2 (Muc2) immunostaining (Fig. S1F,G,H; Fig. 1H).

Goblet cells are the most abundant secretory cells in gut epithelia and maintain the barrier integrity through secretion of intestinal trefoil factor (ITF/TFF3) and Muc2, the major components of gut mucus. The mucus plays dual roles as a lubricant and a physical barrier between luminal contents and the sterile mucosal epithelium (Johansson, et al., 2013). Because of the reduction in mucus-secreting goblet cells, the mucus layers covering the mucosal surface were markedly attenuated in IEC-M14$^{-/-}$ mice (Fig. S1F; Fig. 1H). As a result, luminal bacteria were in close contacts with the mucosal epithelium, and bacterial invasion into the lamina propria space was very common in IEC-M14$^{-/-}$ mice, as revealed by 16S rRNA fluorescent *in situ* hybridization (Fig. 1I). FITC-dextran gavage confirmed increased mucosal permeability in IEC-M14$^{-/-}$ mice (Fig. 1J). As expected, bacterial invasion triggered severe mucosal inflammation. RT-qPCR quantitation confirmed a marked increase in local production of pro-inflammatory cytokines (*Tnfa, Il1b, Il6, Ifng and Il17*) in the IEC-M14$^{-/-}$ colon (Fig. 1K). Western blot analyses confirmed Muc2 and ITF/TFF3 reduction, marked increases in inflammation markers and mediators (TNF-α, HIF-1α, claudin-2) and NF-κB activation (p65(S536) phosphorylation), as well as tight junction dysfunction in IEC-M14$^{-/-}$ mice (Fig. 1L); the latter was manifested by strong induction of myosin light chain (MLC) kinase (MLCK) and MLC phosphorylation, indicators of epithelial tight junction dysfunction (Su, et al., 2013). Furthermore, IEC-M14$^{-/-}$ mice

exhibited dramatic increases in circulating LPS, TNF-α and IL-6 concentrations (Fig. 1M,N), indicating bacterial invasion into the circulation that triggers severe systemic inflammation. Together, these observations suggest that mucosal barrier defects and mucus layer deficiency are the main causes of increased mucosal permeability and bacterial invasion that trigger severe mucosal and systemic inflammation, leading to growth retardation and premature death in IEC-M14$^{-/-}$ mice.

Depletion of gut microbiota in IEC-M14$^{-/-}$ mice reduces inflammation but fails to correct colonic epithelial morphogenesis.

To assess the influence of gut microflora on the colonic abnormalities caused by epithelial m^{6}A depletion, we depleted gut microbiota using antibiotics (Mukherji, et al., 2013). We placed newly weaned M14$^{f/f}$ and IEC-M14$^{-/-}$ mice on drinking water containing an antibiotic cocktail for 6 wks (He, et al., 2019). Compared to untreated IEC-M14$^{-/-}$ mice (Fig. 1A), antibiotic treatment (ABX) markedly improved mouse growth, reduced disease activity index and completely prevented premature death in IEC-M14$^{-/-}$ mice (Fig. S2A,B). ABX also abolished local colonic inflammation (i.e. TNF-α induction and NF-κB activation, Fig. S2C), and markedly diminished systemic inflammation (i.e. circulating TNF-α and IL-6 levels, Fig. S2D). However, ABX failed to correct the aberrant colonic epithelial structure of IEC-M14$^{-/-}$ mice (Fig. S2E). Consequently, ABX-IEC-M14$^{-/-}$ mice still maintained high mucosal permeability and high colonic histological damage scores (Fig. S2F,G). Therefore, gut bacteria play a major role in the development of local and systemic inflammation in IEC-M14$^{-/-}$ mice due to epithelial barrier dysfunction, but have little effects on the aberant colonic epithelial morphogenesis.

Mettl14 deletion with Cdx2-Cre phenocopies the deletion with Villin-Cre.

In IEC-M14$^{-/-}$ mice the villin promoter-driven Cre deletes *Mettl14* from duodenum to distal colon; as such, their severe growth retardation could be due to malnutrition caused by a defective small intestine. To exclude this possibility, we generated M14$^{f/f}$;Cdx2-Cre mice (CEC-M14$^{-/-}$). As Cdx2 promoter directs Cre expression from distal ileum to distal colon in epithelial cells (Hinoi, et al., 2007), CEC-M14$^{-/-}$ mice have intact duodenum and jejunum to maintain normal absorption of nutrients. We confirmed Mettl14 depletion in colonic epithelial cells of CEC-M14$^{-/-}$ mice (Fig. S3A), which led to >60% reduction in the m^{6}A content (Fig. S3B). Like IEC-M14$^{-/-}$ mice, CEC-M14$^{-/-}$ mice suffered severe growth retardation (Fig. S3C) and a very high rate of premature mortality before 10 weeks of age (Fig. S3D). They also had an aberrant colonic mucosal architecture that showed marked depletion of goblet cells and massive immune cell infiltration (Fig. S3E,F,G). As expected, the abnormalities in CEC-M14$^{-/-}$ colon mucosal structure resulted in markedly increased mucosal permeability (Fig. S3H) that led to elevation in LPS and pro-inflammatory cytokine concentrations in the circulation (Fig. S3I,J). Overall, CEC-M14$^{-/-}$ mice closely phenocopied IEC-M14$^{-/-}$ mice. Therefore, the severe phenotypes seen in IEC-M14$^{-/-}$ and CEC-M14$^{-/-}$ mice are unlikely caused by malnutrition, but rather by colonic epithelial barrier abnormalities.

Mettl14 depletion impairs intestinal stem cells.

To understand the cellular and molecular impacts of Mettl14 depletion on colonic epithelial morphogenesis, we performed RNA-seq, m^6A RIP-seq and scRNA-seq. RNA-seq and RIP-seq were carried out using poly(A^+)-RNAs prepared from purified colonic crypts of $M14^{f/f}$ and IEC-$M14^{-/-}$ mice. RNA-seq analysis revealed 3,571 differentially expressed genes (DEGs) in IEC-$M14^{-/-}$ mice ($-0.585>Log_2FC>0.585$, $p<0.05$), among which 2,086 were up-regulated and 1,485 down-regulated (Fig. S4A). RIP-seq showed that m^6A peaks were highly enriched around the stop codon, and the peak motif was identified as 5'G(A)GACU(A)3' ($p=1x10^{-237}$) (Fig. S4B), a highly conserved motif as reported previously (Du, et al., 2020; Dominissini, et al., 2012; Narayan and Rottman, 1988). A total of 9,097 m^6A peaks (associated with 4,417 transcripts) were identified in colonic crypt cells and the majority of these peaks are distributed in the exons and the 3' UTR regions (Fig. S4C). Among these peaks, 7,377 were missing in IEC-$M14^{-/-}$ cells, representing 79.6% reduction. Among the 3,571 DEGs identified from RNA-seq, 1,055 contain m^6A peaks that are associated with $M14^{f/f}$ mice only, and 366 contain peaks that are commonly identified in both $M14^{f/f}$ and IEC-$M14^{-/-}$ mice (Fig. S4D,E).

We performed scRNA-seq using colonic crypt cells pooled from 3 pairs of $M14^{f/f}$ and IEC-$M14^{-/-}$ mice at 5 wks of age. We were able to profile 6,973 $M14^{f/f}$ cells and 4,128 IEC-$M14^{-/-}$ cells. These cells were clustered into 14 clusters (0-13) based on the expression profiles, and these clusters were grouped into seven major cell populations based on known cell-specific markers (Ayyaz, et al., 2019), namely goblet cells (GC), enterocytes (EC), crypt base columnar cells (CBC, which contain the ISC niche) and transit amplifying cells (TAC), enteroendocrine cells (EE), T lymphocytes (T), myeloid cells (M) and B lymphocytes (B) (Fig. S5A,B). Analysis of the scRNA-seq data revealed no quantitative differences in the CBC+TAC populations between $M14^{f/f}$ and IEC-$M14^{-/-}$ mice, but lower GC and EC populations and increased EE, T, M and B populations in IEC-$M14^{-/-}$ mice (Fig. 2A,B). Colonic cell populations from IEC-$M14^{-/-}$ mice showed different expression profiles compared with the $M14^{f/f}$ counterpart (Fig. S5C), which may lead to altered cellular functions. The T, M, and B population data are consistent with severe immune cell infiltration seen in IEC-$M14^{-/-}$ mice. For example, IEC-$M14^{-/-}$ mice showed dramatic increases in *Il1b*-expressing cells in the M population, *Il17a*-expressing cells in the T population and *Iglc*-expressing cells in the B population (Fig. S5D). This is consistent with the RNA-seq data showing the top enriched pathways in IEC-$M14^{-/-}$ cells were related to inflammatory activation (Fig. S4F,G), confirming severe bowel inflammation.

As the inflammatory phenotype is secondary to mucosal barrier dysfunction, we sought to explore the basis for the defect in IEC-$M14^{-/-}$ epithelial barrier. We first examined cell cycle variations and confirmed only the CBC+TAC population expressed genes involved in regulation of cell proliferation (Fig. S5G). Further analysis revealed that S phase markers such as *Pcna, Mcm5* and *Mcm6* were clearly reduced in IEC-$M14^{-/-}$ mice (Fig. S5G–J). Overall, IEC-$M14^{-/-}$ mice had less cells in S phase and more cells in G1 phase in the CBC+TAC population compared to $M14^{f/f}$ mice (Fig. S5K).

As ISCs are proliferating cells, we next examined the ISC populations. The ISC niche is highly plastic and contains different populations. We examined ISCs that express Lgr5,

Olfm4, Clu, Bmi1, Lrig1, Mex3a, Ascl2, Tert or Sox9 in the scRNA-seq and RNA-seq datasets (Fig. 2C,D). The homeostatic regeneration of the intestinal epithelium is driven by $Lgr5^+$ ISCs, the active ISCs located at the crypt base, which give rise to all differentiated epithelial cell types (Barker, et al., 2007). Following injury, the ISC niche undergoes substantial adaptation to exert epithelial repair, potentially by activating the quiescent reserve ISC populations such as $Bmi1^+$ and $Mex3a^+$ CBCs (Santos, et al., 2018), $Hopx^+$ CBCs (Wang, et al., 2019) or the revival ISC population such as Clu^+ CBCs (Ayyaz, et al., 2019). Interestingly, the $Lgr5^+$ ISCs were completely eliminated in the CBC+TAC population of IEC-$M14^{-/-}$ mice; among all quiescent ISCs, Clu^+ cells showed the most dramatic induction in IEC-$M14^{-/-}$ mice (Fig. 2C,D,E). The scRNA-seq and RNA-seq data were consistent in this regard, and Western blot analysis confirmed the loss of Lgr5 and the marked induction of Clu in colonic crypts of IEC-$M14^{-/-}$ mice (Fig. 2F). Clu^+ cells were almost undetectable in $M14^{f/f}$ mice, but became induced in the EC, EE and CBC+TAC populations in IEC-$M14^{-/-}$ mice (Fig. 2E), suggesting that the increase in Clu^+ cells is an adaptation to compensate for the loss of $Lgr5^+$ ISCs to maintain epithelial regeneration.

In this context, we further examined ISC renewal and differentiation using colonic organoid culture, a model system to study the stem cell niche (Kretzschmar and Clevers, 2016). Compared with $M14^{f/f}$ mice, fewer organoids were able to form and grow from colonic crypts isolated from either IEC-$M14^{-/-}$ or CEC-$M14^{-/-}$ mice (Fig. 2G,J). Quantitative analyses revealed substantially lower organoid forming efficiency, lower crypt domains formed per organoid, lower organoid replating efficiency and smaller organoid size in both IEC-$M14^{-/-}$ and CEC-$M14^{-/-}$ mice (Fig. 2H,K). Histological and immunohistological examinations confirmed that the $M14^{-/-}$ organoids were less differentiated with almost no goblet cell formation, and the epithelial layers were thinner and appeared less polarized (Fig. 2G). Importantly, the few surviving $M14^{-/-}$ organoids had completely lost *Lgr5* but expressed a very high level of *Clu* (Fig. 2I). These data strongly suggest that, although Clu^+ cells have reconstituted for the loss of $Lgr5^+$ cells in $M14^{-/-}$ mice, the $M14^{-/-}$ Clu^+ ISCs are most likely defective in their regenerative capability, which at least partially accounts for the impaired epithelial morphogenesis seen in $M14^{-/-}$ colons.

Simultaneous deletion of *Mettl14* from $Lgr5^+$ and Clu^+ cells impaires colon mucosal morphogenesis.

To directly assess the effects of m^6A depletion on $Lgr5^+$ ISCs, we crossed $M14^{f/f}$ mice with Lgr5-EGFP-CreERT2 (Lgr5-CreERT2) mice to obtain $M14^{f/+}$;Lgr5-CreERT2 (as control) and $M14^{f/f}$;Lgr5-CreERT2 mice. The transgenic mice carry GFP that allows for tracking of the $Lgr5^+$ ISCs (Barker, et al., 2007). We first examined colonic organoids. Treatment of $M14^{f/f}$;Lgr5-CreERT2 organoids (but not $M14^{f/+}$;Lgr5-CreERT2 organoids) with 4-hydroxytamoxifen (4-OHT) (but not with EtOH vehicle) eliminated GPF^+ (equivalent to $Lgr5^+$) cells (Fig. 3A), which was associated with a dramatic loss of Lgr5 expression and a marked induction of Clu at both mRNA and protein levels in these organoids (Fig. 3B,C). These data provide direct evidence that Clu^+ cells compensate for the loss of $Lgr5^+$ ISCs in organoids.

We then followed the GFP$^+$ (Lgr5$^+$) cells daily after M14$^{f/f}$;Lgr5-CreERT2 mice were treated with tamoxifen (TAM) to induce *Mettl14* deletion. In contrast to oil vehicle (Oil)-treated mice in which GFP$^+$ (Lgr5$^+$) ISCs were clearly located at the crypt base of the colon, Lgr5$^+$ cells were gradually eliminated over 4 days in the TAM-treated mice (Fig. 3D). RT-qPCR and Western blot analyses confirmed that TAM (but not Oil) completely abolished Lgr5 expression in colonic crypts over 3-4 days, whereas Clu was simultaneously induced (Fig. 3E,F), indicating again that the loss of Lgr5$^+$ ISCs is compensated by Clu$^+$ cells *in vivo*. In this case, the expanded Clu$^+$ population is Mettl14-sufficient; therefore, there were no morphological defects in the colonic mucosal structure of TAM-treated M14$^{f/f}$;Lgr5-CreERT2 mice.

If Clu$^+$ cells indeed expand to compensate for Lgr5$^+$ ISCs in IEC-M14$^{-/-}$ and CEC-M14$^{-/-}$ mice, then Mettl14-deficient Clu$^+$ cells are likely responsible for the aberrant colonic mucosal phenotypes seen in these mice. To test this hypothesis, we set to delete *Mettl14* from both Lgr5$^+$ and Clu$^+$ populations simultaneously. We crossed M14$^{f/f}$;Lgr5-CreERT2 mice with Clu-CreERT2 mice (Ayyaz, et al., 2019) to obtain M14$^{f/f}$;Lgr5-CreERT2;Clu-CreERT2 (M14$^{f/f}$;Lgr5/Clu-CreERT2) mice. Following TAM treatment of adult mice (Fig. 3G), approximately 50% M14$^{f/f}$;Lgr5/Clu-CreERT2 mice died within 16 days (Fig. 3H). As expected, eight days after TAM treatment, colonic epithelial Lgr5 expression was almost completely abolished, whereas Clu was greatly induced in M14$^{f/f}$;Lgr5/Clu-CreERT2 mice (Fig. 3I). Of note, this Clu$^+$ population was Mettl14-deficient. The surviving mice developed aberrant colonic architecture with depletion of goblet cells (Fig. 3J,K), confirmed by reduction of Muc2 protein (Fig. 3I) and other goblet cell markers (Fig. 3L), and massive immune cell infiltration (Fig. 3J), and exhibited a marked elevation of serum pro-inflammatory cytokines (Fig. 3N). These mice also expressed much higher EE markers (Fig. 3M). Therefore, these mice basically phenocopied IEC-M14$^{-/-}$ and CEC-M14$^{-/-}$ mice after TAM-induced Mettl14 depletion. We also generated and examined M14$^{f/f}$;Lgr5-CreERT2;Bmi1-CreERT2 (M14$^{f/f}$;Lgr5/Bmi1-CreERT2) mice and M14$^{f/f}$;Lgr5-CreERT2;Hopx-CreERT2 (M14$^{f/f}$;Lgr5/Hopx-CreERT2) mice, but found no growth abnormalities nor morphological defects in the colonic epithelial structure in these mice (Fig. S6A,B). Therefore, the loss of Lgr5$^+$ ISCs is unlikely compensated by Bmi1$^+$ or Hopx$^+$ cells. These results confirm that Lgr5$^+$ ISCs are reconstituted by Clu$^+$ cell expansion following Mettl14 depletion, but *Mettl14*-ablated Clu$^+$ ISCs are functionally impaired for epithelial regeneration.

Mettl14 depletion triggers excess apoptosis that disrupts colon mucosal morphogenesis.

To explain the rapid loss of Lgr5$^+$ ISCs in the M14$^{-/-}$ epithelium, we examined programmed cell death. TUNEL staining showed that, in contrast to limited apoptosis detected only in terminally differentiated epithelial cells on the luminal surface of the crypts in M14$^{f/f}$ mice, massive apoptosis was seen in both IEC-M14$^{-/-}$ mice (Fig. 4A,B) and CEC-M14$^{-/-}$ mice (Fig. 4C,D), not only in terminal epithelial cells but also in the CBC and TAC regions. Western blot data confirmed the activation of the pro-apoptotic pathway (Puma induction and caspase 3 activation) in colonic crypts from either IEC-M14$^{-/-}$ or CEC-M14$^{-/-}$ mice (Fig. 4E). PUMA induction is a well-known marker of colonic epithelial apoptosis (Qiu, et al., 2011). Excess apoptosis was also seen in the colonic epithelium of one-day old

CEC-M14$^{-/-}$ mice even when the mucosal structure was relatively normal (Fig. 4F,G,H). We also examined the M14$^{f/f}$;Lgr5-CreERT2 mice and found numerous TUNEL-positive cells at the crypt base of the colon two days following TAM induction (Fig. 4I), confirming that disruption of Lgr5^{+} ISCs is caused by excess apoptosis.

To confirm that excess apoptosis causes aberrant colonic morphogenesis, we generated M14$^{f/f}$;Cdx2-CreERT2 mice. In M14$^{f/f}$;Cdx2-CreERT2 colonic organoids, 4-OHT treatment triggered time-dependent apoptosis within 4 days (Fig. 4J,K). Western blot analyses confirmed time-dependent activation of the pro-apoptotic pathway (Puma induction and activation of caspase 3 and 9), as well as time-dependent depletion of Mettl14, loss of Muc2 and Lgr5 and induction of Clu in these organoids following 4-OHT treatment (Fig. 4L). However, co-treatment of these organoids with Q-VD-OPh, a pan caspase inhibitor, blocked apoptosis (Fig. 4M) and the pro-apoptotic signaling (Fig. 4N), as well as prevented Lgr5 and Muc2 depletion and Clu induction (Fig. 4N). Moreover, Q-VD-OPh also blocked Lgr5 depletion and Clu induction and prevented apoptosis in M14$^{f/f}$;Lgr5-CreERT2 (Fig. 4O) and M14$^{f/f}$;Lgr5/Clu-CreERT2 organoids (Fig. 4P,Q), confirming that disruption of the Lgr5^{+} ISCs is caused by apoptosis.

To explore the *in vivo* effect of excess apoptosis on colonic morphogenesis, we treated adult M14$^{f/f}$;Cdx2-CreERT2 mice with Q-VD-OPh following TAM-induced Mettl14 depletion. As expected, TAM caused >50% mortality of M14$^{f/f}$;Cdx2-CreERT2 mice within two weeks, and these mice exhibited abnormal colonic mucosal structure, increased mucosal permeability and elevated serum LPS concentration, which mimicked the phenotypes of CEC-M14$^{-/-}$ mice; however, all these abnormalities were completely blocked by Q-VD-OPh treatment (Fig. 4R,S,T,U). At the molecular level, Q-VD-OPh blocked Lgr5 disruption and Puma and caspase 3 activation in the colonic epithelial cells (Fig. 4V). Together, these observations indicate that excess apoptosis triggered by Mettl14 depletion is the cause of Lgr5^{+} ISC disruption and aberrant colon mucosal morphogenesis.

GsdmC2/3/4 are Mettl14-targeted transcripts that regulate apoptosis.

To search for Mettl14-targeted transcripts we integrated the RNA-seq, RIP-seq and scRNA-seq data for analysis. RNA-seq data showed that *GsdmC2, GsdmC3* and *GsdmC4* were the most down-regulated transcripts in IEC-M14$^{-/-}$ colonic epithelial cells (Fig. 5A,B), whereas no other Gsdm family members were down-regulated in IEC-M14$^{-/-}$ mice. Mice have four *GsdmC* gene copies (*GsdmC1/2/3/4*) tandemly arranged on chromosome 15 (Tamura, et al., 2007). RIP-seq showed that *GsdmC1* transcript is not methylated, whereas *GsdmC2/3/4* transcripts are heavily methylated, but their methylation was drastically reduced in IEC-M14$^{-/-}$ mice (Fig. 5C). scRNA-seq data revealed that *GsdmC1* is not expressed in the colon, whereas *GsdmC2/3/4* are highly expressed in the EC and CBC+TAC populations, but their expression was drastically diminished in IEC-M14$^{-/-}$ mice (Fig. 5D, Fig. S7A). These analyses strongly suggest that *Gsdmc2/3/4* are the top potential target transcripts of Mettl14 in the colon. We confirmed by RT-qPCR and Western blotting that GsdmC1 was undetectable in purified M14$^{f/f}$ colonic epithelial cells and GsdmC2/3/4 were reduced to undetectable levels in IEC-M14$^{-/-}$ or CEC-M14$^{-/-}$ colonic epithelial cells (Fig. 5E,F,G).

We also confirmed by m^{6}A IP-qPCR that the methylation on the 3' exons of *GsdmC2/3/4* transcripts was almost completely depleted in IEC-M14$^{-/-}$ colonic epithelial cells (Fig. 5H).

As *Mettl14* deletion induced a dramatic down-regulation of *GsdmC2/3/4* in the CBC+TAC populations (Fig. 5D, Fig. S7A), we speculated that GsdmC2/3/4 regulate the ISCs. Indeed, in M14$^{f/f}$;Cdx2-CreERT2 organoids, 4-OHT-induced *Mettl14* deletion led to time-dependent down-regulation of *GsdmC2/3/4* transcripts and GsdmC protein, and this was associated with depletion of *Muc2* and *Lgr5* and induction of *Clu* (Fig. 5I,J). Mettl14 depletion in Lgr5-expressing cells also led to GsdmC down-regulation (Fig. 5P,Q, see lanes with + Ctrl-lentivirus). In fact, Mettl14 depletion promoted *GsdmC2/3/4* mRNA decay and completely eliminated new GsdmC protein synthesis in colonic organoids (Fig. S7B,C). Interestingly, the basal GsdmC expression was much lower in the small intestines than in the colon at both mRNA and protein levels, and only colonic GsdmC expression was drastically down-regulated by *Mettl14* deletion (Fig. S7D,E). If *GsdmC* is a Mettl14 target, then these observations explain why IEC-M14$^{-/-}$ mice developed severe abnormalities only in the colon but not in the small intestine.

To confirm that GsdmC indeed functionally acts downstream of Mettl14 to regulate epithelial apoptosis, we tested whether ectopically forced expression of GsdmC is able to rescue M14$^{-/-}$ cells from apoptosis. To this end, we transduced M14$^{f/f}$;Cdx2-CreERT2 organoids with lentivirus that expresses human GSDMC (GSDMC-lentivirus) or METTL14 (METTL14-lentivirus) before 4-OHT induction; the latter served as the positive control. As expected, METTL14-lentivirus transduction restored METTL14 in 4-OHT treated organoids (Fig. 5K) and prevented 4-OHT-induced apoptosis as seen in the Ctrl-lentivirus transduced organoids (Fig. 5L); moreover, METTL14 transduction also restored the expression of GsdmC, Lgr5 and Muc2 while blocking the induction of Clu and Puma and caspase 3 activation (Fig. 5K). Importantly, GSDMC-lentivirus transduction of M14$^{f/f}$;Cdx2-CreERT2 organoids also completely prevented 4-OHT-induced apoptosis, blocked caspase 3 activation, and restored Lgr5 expression without altering the Mettl14 status (Fig. 5M,N). Morphologically, GSDMC transduction of these organoids restored the mucus-producing goblet cells (Fig. 5O) that were completely missing in the surviving IEC-M14$^{-/-}$ organoids (see Figure 2G) (Ctrl-lentivirus transduced M14$^{f/f}$;Cdx2-CreERT2 organoids could not be obtained for Alcian blue staining as they did not survive 4 days after 4-OHT induction). Furthermore, GSDMC transduction also rescued M14$^{f/f}$;Lgr5-CreERT2 organoids and M14$^{f/f}$;Lgr5/Clu-CreERT2 organoids from Lgr5 depletion (thus preventing Clu induction) and apoptosis (Fig. 5P,Q,R), indicating that GsdmC directly regulates the Lgr5$^+$ ISCs.

To further prove that Mettl14 targets GsdmC *in vivo*, we generated two lines of transgenic (Tg) mice that carry villin promoter-driven human GSDMC cDNA coding sequence (Fig. S7F,G), and both Tg lines expressed GSDMC throughout the intestine (Fig. S7H,I). The expression level of GsdmC/GSDMC in the colon of both Tg lines was estimated to be double the endogenous GsdmC level in wildtype (WT) littermates (Fig. S7I). When we crossed these hGSDMC-Tg mice with CEC-M14$^{-/-}$ mice, all abnormalities seen in CEC-M14$^{-/-}$ mice were completely rescued in CEC-M14$^{-/-}$;GSDMC offspring from both Tg lines (Fig. 5S; Fig. S7J), including growth retardation, premature death, aberrant colonic mucosal structure and excess apoptosis (Fig. 5S–W). At the molecular level, the GSDMC

transgene restored GSDMC expression in the presence of Mettl14 depletion, prevented Lgr5 loss and blocked pro-apoptotic signaling activation and Clu induction in these “rescued” mice (Fig. 5X). Taken together, these data provide compelling evidence that *GsdmC2/3/4* are direct Mettl14 targets and GsdmC acts downstream of Mettl14 to regulate the colonic ISC niche and prevent apoptosis.

GsdmC maintains mitochondrial integrity.

In scRNA-seq data analysis we noticed that IEC-M14$^{-/-}$ colonic crypt cells contained much higher levels of intracellular mitochondrial RNAs compared with M14$^{f/f}$ counterparts (Table S1), suggesting intrinsic mitochondrial instability or mitochondrial “leak” in IEC-M14$^{-/-}$ cells. Therefore, to explore the mechanism whereby GsdmC depletion triggers apoptosis, we examined mitochondria, as cytochrome c release from mitochondria is the most important initiator of apoptosome formation (Tait and Green, 2013; Riedl and Salvesen, 2007). In both IEC-M14$^{-/-}$ and CEC-M14$^{-/-}$ colonic epithelial cells, staining with a mitochondrial fluorescent probe MitoTracker revealed disrupted mitochondrial morphology (Fig. 6A). Exposure of these mutant cells to JC-1 dye, a mitochondrial potential sensor, revealed severe mitochondrial depolarization, as was indicated by dramatic decreases in the ratio of red/green fluorescence intensity (Fig. 6B,C). Western blot analyses of cytosolic and mitochondrial fractions indicated that GsdmC was highly associated with mitochondria, but *Mettl14* deletion completely abolished the mitochondrial GsdmC, and this loss was associated with cytochrome c release from mitochondria into the cytosolic compartment; meanwhile, Mettl14 depletion also stimulated Fis1 recruitment to mitochondria and induced Drp1 phosphorylation (Fig. 6D,E), which are part of the machinery to drive mitochondrial fission (Zhan, et al., 2013). Importantly, in M14$^{f/f}$;Cdx2-CreERT2 organoids, 4-OHT treatment also disrupted mitochondrial structure and induced mitochondrial depolarization (Fig. 6F,G,H). Western blotting confirmed that 4-OHT induced GsdmC depletion and cytochrome c release from mitochondria and stimulated mitochondrial Fis1 recruitment and Drp1 activation in a time-dependent manner (Fig. 6I,J). Lentiviral transduction of M14$^{f/f}$;Cdx2-CreERT2 organoids with METTL14 or GSDMC blocked cytochrome c release, Fis1 recruitment and Drp-1 phosphorylation induced by 4-OHT (Fig. 6K,L,M,N). Moerover, the GSDMC transgene was able to prevent mitochondrial depolorization (Fig. 6O,P) and block mitochondrial cytochrome c release and Fis recruitment in the “rescued” mice (Fig. 6Q,R). In contrast, blockade of caspase activation with Q-VD-OPh had no effects on these changes in either TAM-treated M14$^{f/f}$;Cdx2-CreERT2 mice (Fig. 6S,T) or 4-OTH-treated M14$^{f/f}$;Cdx2-CreERT2 organoids (Fig. 6U,V), because caspases function down-stream of cytochrome c in the death cascade (Tait and Green, 2013). These observations indicate that GsdmC functions to maintain mitochondrial membrane potential and protect mitochondrial integrity.

GSDMC knockdown triggers apoptosis in human colonic organoids and colon cancer cells.

Finally, we used human colonic organoids and human colon cancer cells to directly test whether GSDMC depletion would trigger apoptosis independent of METTL14. We knocked down human GSDMC via RNA interference. When human colonic organoids were transduced by GSDMC-shRNA-lentivirus that co-expresses GFP, massive apoptosis

was induced on day 3 following transduction, and the dying cells lost GFP expression as expected (Fig. 7A,B). We confirmed that in these transduced organoids METTL14 expression was not affected, but Lgr5 expression was abolished whereas Clu was highly induced, and the pro-apoptotic pathway (PUMA, caspase 3 and 9) was markedly activated (Fig. 7C). Western blot analyses of mitochondrial and cytosolic fractions further confirmed GSDMC depletion, Fis1 and Drp1 activation and cytochrome c release from mitochondria into cytosol in these organoids following GSDMC-shRNA transduction (Fig. 7D,E).

We further demonstrated that transfection of HCT116 human colon cancer cells with GSDMC-siRNA induced mitochondrial depolarization (Fig. 7F,G), and transduction of these cells with GSDMC-shRNA-lentivirus induced apoptosis (Fig. 7H). This is highly unusual, as HCT116 cells are notoriously resistant to apoptosis. Interestingly, when GSDMC-shRNA-transduced HCT116 cells were treated with TNF-α, which is known to activate the pro-apoptotic pathway without inducing apoptosis in these cancer cells, massive apoptosis developed (Fig. 7H). At the molecular level, we confirmed that knockdown of METTL14 led to GSDMC reduction and activation of the pro-apoptotic pathway (PUMA, Caspase 3 and 9) in HCT116 cells (Fig. 7I), whereas direct silencing of GSDMC also triggered the pro-apoptotic pathway, mitochondrial fission and cytochrome c release, without altering METTL14 expression (Fig. 7J,K,L). Together, these data confirm that depletion of GsdmC/GSDMC indeed triggers cytochrome c-mediated apoptosis in mice and humans.

Discussion

In this study we show that gut epithelial m^6A depletion leads to aberrant mucosal morphogenesis that causes spontaneous colonic and systemic inflammation, severe growth retardation and pre-mature death in mice. One major defect is a remarkable reduction of functional goblet cells required for mucus production. Insufficient mucus secretion disrupts the formation of the protective mucus layers. In addition, tight junction dysfunction caused by Mettl14 depletion further compromises the epithelial barrier. Consequently, the lack of mucus protection and increased barrier permeability result in massive luminal bacterial invasion that triggers severe colonic and systemic inflammation; the latter is evidenced by marked increases in serum LPS and pro-inflammatory cytokines in the mutant mice. Mouse growth retardation and pre-mature death are caused by bacteria-triggered inflammation, but unlikely by malnutrition from potential defects in the small intestine. Bacterial depletion reduces inflamamiton but can not rescue the colonic architecture of the mutant mice, suggesting the epithelial abnormalities caused by m^6A depletion is independent of inflammation. Moreover, our data exclude confounding developmental effects on the phenotypes, because adult mice develop severe abnormalities within 2-3 weeks following tamoxifen-induced *Mettl14* deletion. To some extent the phenotype caused by Mettl14 depletion is similar to that of *Muc2* knockout mice, which also develop growth retardation and spontaneous colitis because of bacterial invasion (Van der Sluis, et al., 2006). These two models confirm the importance of goblet cells and mucus production in the maintenance of the colonic epithelial barrier.

Gut mucosal homeostasis is maintained by constant epithelial regeneration driven by the ISC niche. Here we show that the most important impact of epithelial m^6A depletion at

the cellular level is on the $Lgr5^+$ and Clu^+ ISCs, and that is likely the primary cause of aberrant colonic morphogenesis in $M14^{-/-}$ mice. The $Lgr5^+$ ISCs are the active ISCs at the crypt base that are responsible for the replenishment of the entire mucosal epithelial lineages under normal conditions (Barker, et al., 2007). However, the ISC niche is highly plastic and contains quiescent "+4" ISCs that are capable of rapid expansion to maintain epithelial homeostasis following injury. For example, $Bmi1^+$ reserve stem cells proliferate to repopulate damaged crypts and villi of the small intestine after high dose radiation injury (Yan, et al., 2012; Sangiorgi and Capecchi, 2008), $Hopx^+$ cells are colitis-associated regenerative stem cells contributing to mucosal repair (Wang, et al., 2019; Takeda, et al., 2011), and Clu^+ revival stem cells can transiently expand to reconstitute the $Lgr5^+$ compartment and regenerate the intestinal epithelium after injury (Ayyaz, et al., 2019). Interestingly, our data from both scRNA-seq and RNA-seq reveal that the most dramatic cellular changes caused by m^6A depletion occur in the $Lgr5^+$ and Clu^+ cell populations – a complete depletion of the $Lgr5^+$ ISCs and a simultaneous robust increase in the Clu^+ population in the colonic epithelium; the latter is extremely rare and almost undetectable under normal conditions (Ayyaz, et al., 2019). These observations support a notion that the Clu^+ ISCs reconstitute the $Lgr5^+$ compartment following epithelial m^6A depletion. Therefore, the Mettl14-deficienct Clu^+ ISCs are responsible for the aberrant epithelial phenotype in the $M14^{-/-}$ mice. Our evidence from two models supports this notion. One model carries *Mettl14* deletion in Lgr5-expressing cells that shows robust Clu induction but normal colonic epithelium, and the other has *Mettl14* deletion simultaneously from both $Lgr5^+$ and Clu^+ populations that exhibits robust Clu induction as well as impaired colonic morphogenesis characteristic of IEC-$M14^{-/-}$ and CEC-$M14^{-/-}$ mice. Taking a similar genetic approach, we exclude the involvement of $Bmi1^+$ or $Hopx^+$ ISCs in the compensation of $Lgr5^+$ ISCs in the presence of m^6A depletion. Collectively, these data demonstrate that RNA m^6A plays an essential role in $Lgr5^+$ ISC survival and self-renewal and in maintaining the differentiation potential of the Clu^+ ISCs.

The underlying cause of $Lgr5^+$ ISC depletion is m^6A depletion-induced apoptosis. The pro-apoptotic pathway is markedly activated in colonic crypt cells and organoids following *Mettl14* deletion from the mucosal epithelial cells or from only the $Lgr5^+$ and Clu^+ cell populations. The excess apoptosis induced by Mettl14 depletion compromises the colonic mucosal barrier and is responsible for the severe inflammatory phenotype of $M14^{-/-}$ mice, because blockade of apoptosis not only rescues the $Lgr5^+$ ISCs and inhibits Clu induction, but also normalizes the mucosal epithelial structure, corrects the leaky mucosal barrier and completely prevents the pre-mature death of $M14^{-/-}$ mice. There are several interpretations for these observations: (1) In addition to depleting the active $Lgr5^+$ ISCs, excess apoptosis in the non-ISC populations disrupts the balance between cell death and proliferation in mucosal epithelial morphogenesis leading to formation of aberrant epithelial barrier; (2) The Mettl14-depleted Clu^+ cells that are induced to replace $Lgr5^+$ ICSs in $M14^{-/-}$ mice are compromised in their regenerative capacity, thus resulting in abnormal epithelium. When apoptosis is inhibited in $M14^{-/-}$ mice, $Lgr5^+$ compartment is kept intact and functions normally; consequently, there is no need for the $Lgr5^+$ to Clu^+ transition.

Through integrated bioinformatic analyses we identified *GsdmC* transcripts as the molecular target of m^6A methyltransferase whose dramatic reduction is responsible for the excess

apoptosis seen in the M14$^{-/-}$ colonic epithelium. This totally unexpected discovery overturns our original speculation that Mettl14 may target the Wnt, Notch or BMP pathways, as these pathways are well known to play critical roles in ISC renewal and intestinal morphogenesis (Perochon, et al., 2018; Sancho, et al., 2015; Noah and Shroyer, 2013; Gregorieff and Clevers, 2005). The Gsdm family consists of GsdmA/B/C/D/E and Pejvakin, and they are exclusively expressed in the epithelium of the skin and gastrointestinal tract (Feng, et al., 2018; Tamura, et al., 2007). The function of the Gsdm family was unknown until 2015 when GsdmD was identified as a key regulator promoting pyroptotic cell death (Liu, et al., 2016; Kayagaki, et al., 2015; Shi, et al., 2015). Under inflammasome stimulation, GsdmD is cleaved to N-terminal and C-terminal fragments by caspase 1, 4, 5 or 11, and the cytotoxic N-terminal domain then inserts into cell membranes to form oligomeric pores that induce pyroptosis (Broz, et al., 2020). Subsequently, GsdmA, B and E were also found to regulate pyroptosis and anti-cancer immunity (Wang, et al., 2020a; Zhang, et al., 2020; Zhou, et al., 2020; Ding, et al., 2016), and human GSDMC was reported to control the switch from apoptosis to pyroptosis in cancer cells (Hou, et al., 2020). In contrast to the other members of the Gsdm family, our data suggest that the normal function of GsdmC/GSDMC in the colonic epithelium is to maintain mitochondrial integrity and prevent apoptotic cell death, because GsdmC down-regulation disrupts mitochondrial membrane potential and triggers excessive epithelial apoptosis, which is the primary cause for the severe phenotypes seen in M14$^{-/-}$ mice. Most recently, GSDMB was also reported to have non-pyroptotic functions in the colon (Rana, et al., 2022).

While *GsdmC1* transcript is not m^{6}A-methylated nor expressed in the colon, *GsdmC2/3/4* transcripts are highly expressed in colonic CBC, TAC and EC populations, and the CBC contains the ISC niche. We found that these transcripts are the most down-regulated in M14$^{-/-}$ colonic crypt cells, and the down-regulation is associated with depletion of m^{6}A peaks from these transcripts. We confirmed that *Mettl14* deletion depletes *GsdmC2/3/4* methylation, promotes the decay of their transcripts and completely abolishes new GsdmC protein synthesis. The evidence to support *GsdmC2/3/4* as the down-stream functional targets of Mettl14 is that forced expression of GsdmC is able to block the activation of the pro-apoptotic pathway and rescue M14$^{-/-}$ organoids from apoptosis without changing the Mettl14-deficient status. Another compelling evidence is that the GSDMC transgene is able to completely rescue M14$^{-/-}$ mice from developing growth retardation, premature death, colonic epithelial abnormalities, Lgr5^{+} ISC loss and mitochondrial dysfunction without changing the Mettl14-deficient status. We further demonstrated that GSDMC knockdown not only activates the pro-apoptotic pathway but also induces robust apoptosis in human colonic organoids and colon cancer cells, confirming that GsdmC depletion triggers apoptosis independent of Mettl14.

How GsdmC depletion triggers apoptosis? We found that GsdmC is associated with mitochondria, and depletion of GsdmC from mitochondria disrupts mitochondrial membrane potentials and triggers mitochondrial fission, cytochrome c release into the cytosolic compartment and caspase 3 and 9 activation. Cytochrome c is the initiator of apoptosome formation by Apaf-1 and procaspase 9, which activates caspase 9 in the death cascade (Tait and Green, 2013; Riedl and Salvesen, 2007). Cytochrome c release may be a result of mitochondrial outer membrane permeabilization or asymmetrical mitochondrial fission that

sequesters and eliminates damaged organelle components (Shirihai, et al., 2015; Zhan, et al., 2013). These findings prompt us to speculate that GsdmC is a crucial mitochondrial stabilizer. This is a previously unknown feature of the Gsdm family, but how GsdmC maintains mitochondrial integrity and regulates mitochondrial functions requires further investigation.

In summary, we demonstrate that N^6-adenosine methyltransferase plays an essential role in colonic epithelial morphogenesis and regeneration by regulating the stability of *GsdmC* transcripts. Our work suggests that in m^6A depletion, GsdmC down-regulation triggers cytochrome c-mediated programmed cell death that depletes $Lgr5^+$ ISCs and causes adaptive expansion of Clu^+ ISCs, and Mettl14-deficient Clu^+ ISCs lose normal regenerative capacity leading to aberrant colonic morphogenesis and severe inflammation in $M14^{-/-}$ mice.

Limitation of the Study

It remains unclear why Clu^+ ISCs are resistant to apoptosis in the absence of Mettl14 or GsdmC. We do not yet fully understand the basis for the impact *Mettl14* ablation or GsdmC depletion on enterocytes and enteroendocrine cells, given that GsdmC is highly enriched in enterocytes (Fig. S7A) and Mettl14 is enriched in some enteroendocrine cells (not shown). It is also unclear what reader protein(s) interact with *GsdmC* m^6A sites to regulate *GsdmC* degradation. An ideal experiment would be to mutate the key *GsdmC* m^6A sites to prove the functionality of the Mettl14-m^6A axis in *GsdmC* regulation. Finally, it is plausible that Mettl14 regulates *GsdmC* via another Mettl14 target. These questions warrant future investigation.

RESOURCE AVAILABILITY

Lead Contact

- Further information and requests for resources and reagents should be directly addressed to and will be fulfilled by lead contact, Yan Chun Li (cyan@medicine.bsd.uchicago.edu).

Materials Availability

- Lentiviruses and plasmid DNA constructs generated in this study will be available from the corresponding author upon request.
- Transgenic mouse lines generated in this study will be available from the corresponding author upon request.

Data and Code Availability

- All datasets (scRNA-seq, RIP-seq, RNA-seq) generated in this study have been deposited at GEO under the accession numbers GSE181928, GSE181863 and GSE181927, respectively, and are publicly available as of the date of publication.
- Any additional information required to reanalyze the data reported in this paper is available from the lead contact upon request.

- Orignal Western blot images and microacopy data reported in this paper will be shared by the lead contact upon request.

EXPERIMENTAL MODEL AND SUBJECT DETAILS

Animals

Mettl14$^{flox/flox}$ mice carrying two LoxP sites flanking exons 7-9 in the *Mettl14* gene have been described previously (Du, et al., 2020). Villin-Cre transgenic mice (B6,Cg-Tg(Vil-Cre)1000Gum/J; Stock # 021504), CDX2-Cre transgenic mice (B6.Cg-Tg(CDX2-cre)101Erf/J; Stock # 009350), CDX2-CreERT2 mice (B6.Cg-Tg(CDX2-Cre/ERT2)752Erf/J; Stock # 022390), Lgr5-EGFP-IRES-CreERT2 mice (B6.129P2-*Lgr5*$^{tm1(cre/ERT2)Cle}$/J; Stock #: 008875), Bmi1-CreERT transgenic mice (B6;129-*Bmi1*$^{tm1(cre/ERT)Mrc}$/J; Stock #010531) and Hopx-CreERT2 transgenic mice (*Hopx*$^{tm2.1(cre/ERT2)Joe}$/J; Stock #: 017606) were purchased from Jackson Laboratory. Clu-CreERT2 transgenic mice were provided by Alex Gregorieff (Ayyaz, et al., 2019). These mice were used to breed and produce *Mettl14*$^{flox/flox}$;Villin-Cre (IEC-M14$^{-/-}$), *Mettl14*$^{flox/flox}$;CDX2-Cre (CEC-M14$^{-/-}$), *Mettl14*$^{flox/flox}$;CDX2-CreERT2 (M14$^{f/f}$;Cdx2-CreERT2), *Mettl14*$^{flox/flox}$;Lgr5-EGPF-CreERT2 (M14$^{f/f}$;Lgr5-CreERT2), *Mettl14*$^{flox/flox}$;Lgr5-EGPF-CreERT2;Clu-CreERT2 (M14$^{f/f}$;Lgr5/Clu-CreERT2), *Mettl14*$^{flox/flox}$;Lgr5-EGPF-CreERT2;Bmi1-CreERT2 (M14$^{f/f}$; Lgr5/Bmi1-CreERT2), and *Mettl14*$^{flox/flox}$;Lgr5-EGPF-CreERT2;Hopx-CreERT2 (M14$^{f/f}$;Lgr5/Hopx-CreERT2) mice.

Human GSDMC cDNA was PCR-amplified and placed down-stream of 12.4 kb villin gene promoter. The amplified GSDMC cDNA sequence was validated by DNA sequencing. hGSDMC transgenic (Tg) mice were produced by microinjecting the PmeI DNA fragment that contains 12.4kb villin promoter-driven 1.6kb human GSDMC cDNA (Fig. S7F) into the pronucleus of C57BL/6 mouse embryos, and these embryos were thereafter implanted into the oviducts of pseudopregnant surrogate mothers. A total of 19 pups were obtained following the microinjection, of which two transgenic founders (#7 and #15) were identified by tail DNA PCR using hGSDMC-specific primers. Breeding of these founders with wildtype (WT) C57BL/6 mice resulted in transmission of the hGSDMC transgene in two Tg lines (#7 and #15). Expression of hGSDMC in intestinal epithelial cells of these two Tg lines was confirmed by RT-PCR and Western blotting analyses. Both lines were crossed with *Mettl14*$^{flox/+}$;CDX2-Cre mice to generate CEC-M14$^{-/-}$ mice that carried the GSDMC transgene (CEC-M14$^{-/-}$;GSDMC).

All mice were housed at 25°C and maintained in a 12h/12hr light/dark cycle. Both male and female were used in experiments. Mouse disease activity index was assessed based on the extent of diarrhea, bleeding and lethargy as previously described (Van der Sluis, et al., 2006). To deplete gut microbiota, some mice were fed drinking water containing an antibiotic cocktail (ampicillin 1g/L; vancomycin 500 mg/L; neomycin sulfate 1g/L; metronidazole 1g/L) for up to 6 weeks right after weaning as previously reported (Du, et al., 2017; Rakoff-Nahoum, et al., 2004). To activate CreERT2 activity, some mice were intraperitoneally injected with up to three doses of tamoxifen (TAM) (one dose = 0.1ml at 10 mg/ml). Injection of corn oil (Oil) served as control. To block gut epithelial apoptosis, some

mice were treated with Q-VD-OPh via intraperitoneal injection at 8 mg/kg twice per day. All animal study protocols were approved by the Institutional Animal Care and Use Committee at the University of Chicago.

Cell lines

HCT116 cell line (CRL-247) was purchased from ATCC. These cells were cultured in DMEM supplemented with 10% heat-inactivated fetal bovine serum (FBS), 100 U/ml penicillin and 100 μg/ml streptomycin at 37°C and 5% CO_2.

METHOD DETAILS

Mucosal permeability

Mouse gut mucosal permeability was assessed using FITC-dextran as reported previously (Du, et al., 2015). Mice were fasted for 6 hours before being orally gavaged with 4,000 Da FITC-dextran (Sigma-Aldrich) at 200 mg/kg. After 2.5 hours, blood was collected from the tail, and serum FITC-dextran contents were measured at 530 nm wavelength using a BioTek Synergy H1 Hybrid microplate reader.

Serum LPS quantitation

Mouse serum LPS concentrations were quantified using an LPS ELISA kit from LifeSpan Technologies according to the manufacturer's instructions.

Serum cytokine quantitation

Mouse TNF-α, IL-6, IL-1β and IFN-γ concentrations in the sera were quantified using ELISA kits purchased from BioLegend according to the manufacturer's instructions.

Myeloperoxidase (MPO) activity

Colonic lysate MPO activity was determined as described previously (Du, et al., 2015). Briefly, colon tissues were homogenized in 50 mM potassium phosphate and 50 mM hexadecyl trimethyl ammonium bromide (HTAB), sonicated, snap frozen and thawed twice, followed by addition of 50 mM potassium phosphate containing 0.167 mg/ml O-dianisidine dihydrochloride and 0.0005% hydrogen peroxide. Absorbance was read at 460 nm using an EL800 Universal Microplate Reader (BioTek Instruments).

Histology, immunohistochemical and immunofluorescent staining

Colons were harvested immediately after mice were killed. The colons were cut longitudinally, washed with ice-cold PBS and prepared as "Swiss rolls" (Park, et al., 1987) for fixation overnight in 4% formaldehyde made in PBS (pH 7.2) or Carnoy's solution at room temperature. The colon tissues were processed, embedded in paraffin wax and cut into 4 μm sections. The sections were stained with hematoxylin and eosin (H&E) for routine structural examination. Alcian blue staining was used to examine mucus production by goblet cells using commercial kits according to the manufacturers' protocols (Vector Laboratories and IHC WORLD). For immunostaining, sections were boiled in 10mM sodium citrate (pH 6.0) for 10-15 min for antigen retrieval before being stained with

primary antibodies. After washes, the sections were continuously incubated with horseradish peroxidase (HRP)-conjugated secondary antibodies and the antigens were visualized by incubating with 3,3'-diaminobenzidine as substrate. Or the sections were incubated with fluorescence-conjugated secondary antibodies and observed under a confocal fluorescent microscope. To visualize GFP, the colon Swiss rolls were embedded in OCT media (ThermoFisher), frozen on dry ice and cut to 5 μm frozen sections using a cryostat. The slides were observed under a fluorescent microscope.

Assessment of apoptosis

Colonic epithelial apoptosis was assessed by TUNEL staining using an *In Situ* Cell Death Detection Kit (Roche) according to the manufacturer's protocol. Apoptosis was semi-quantified as TUNEL-positive cells per crypt by counting TUNEL-positive cells from randomly selected 50 colonic crypts in each animal. Apoptosis in colonic organoids or cell cultures was assessed by propidium iodide (PI) staining by adding PI (1 μg/ml) into the media as described previously (Wang, et al., 2020b). PI positive areas observed under a fluorescent microscope were quantified using Image J software (NIH).

Bacterial 16S rRNA fluorescent *in situ* hybridization (FISH)

Freshly collected large intestines with fecal pellets were carefully cut into 3-5 mm sections, which were fixed *en masse* in Carnoy's solution overnight, processed, embedded in paraffin and cut to 5 μm sections. For FISH, the sections were deparaffinized, dried and incubated with the fluorescent oligonucleotide probe Alexa 647 5'-GCTGCCTCCCGTAGGAGT-3' (IDT EUB338) at a final concentration of 1ng/μl dissolved in hybridization buffer (0.9 M NaCl, 20 mM Tris-HCl pH7.5, 0.01% SDS, 35% formamide) overnight at 50°C in a dark and humidified Tupperware container. After hybridization, the slides were washed 3x for 15min each wash in prewarmed wash buffer (80 mM NaCl, 20 mM Tris-HCl pH7.5, 5 mM EDTA, 0.01% SDS) at 50°C. The slides were then air dried, counterstained with DAPI for 1 min, and mounted using ProLong Gold Antifade Reagent (Molecular Probes). The slides were observed under a Super-Resolution Laser-Scanning confocal microscope (Leica SP5 II STED-CW) and captured images analyzed using ImageJ software (NIH).

Mitochondrial assessment

Mitochondrial membrane potential was assessed by fluorescent staining with MitoTracker probe (Cell Signaling) and JC-1 dye (MitoProbe JC-1 Assay Kit, ThermoFisher) according to the manufacturers' instruction. Flow cytometric analysis for JC-1-stained cells was performed in a BD LSRFortessa unit (BD Biosciences) and data analyzed by FlowJo software V10. To analyze mitochondrial proteins, mitochondrial and cytosolic fractions were prepared using a Mitochondria Isolation Kit (ThermoFisher) according to the manufacturer's protocol.

Colonic organoid cultures

Mouse and human colonic organoids were prepared and grown on Matrigel (Corning) using StemCell Technologies media based on protocols provided by StemCell Technologies with some modifications. Briefly, freshly harvested colons were placed in a 10 cm dish containing

5 ml of cold PBS (Ca^{++} and Mg^{++} free), cut longitudinally and rinsed 3x times with ice-cold PBS. Then the tissues were cut into 2 mm pieces in 15 ml of cold PBS containing 10 mM EDTA in a 50 ml conical tube using scissors, followed by 45 min rotation (45 rpm/min) in cold room. After rotation, the tissues were precipitated by centrifugation at 4°C for 5 min (290 x g) and washed with cold PBS. Then the pieces were resuspended in 1 ml cold PBS containing 0.1% BSA and pipetted up and down 40 times using a pre-wetted 1 ml pipettor to make the supernatant cloudy. The supernatant was then passed through 70-μm filters to enrich crypts, followed by centrifugation at 290 x g for 5 minutes at 4°C. The pellet was resuspended in cold DMEM/F-12 containing 15 mM HEPES, and the number of crypts was counted. The suspension was centrifuged again at 290 x g for 5 minutes at 4°C to precipitate crypts. The crypts then were resuspended in Matrigel uniformly at 500 crypts/50 μl Matrigel, placed into a pre-warmed 24-well plate and incubated at 37°C for 20 min. After the Matrigel became solidified, pre-warmed complete Mouse IntestiCult™ Organoid Growth Medium (for mouse tissues) or Human IntestiCult Organoid Growth Medium (for human tissues) was added and the plate cultured at 37°C and 5% CO_2. The medium was changed every 2 days. For passage and replating, the mouse colonic organoids were dissociated with the Gentle Cell Dissociation Reagent (StemCell Technologies) and re-cultured under the same condition. Human colon surgical tissues were obtained from The University of Chicago Medical Center with informed consent under an IRB protocol approved by the University Medical Center Institutional Review Boards.

Lentiviral constructs and transduction

METTL14-lentivirus has been described previously (Du, et al., 2020). Lentivirus that expresses GSDMC was constructed by cloning the coding region of human *GSDMC* [NM_031415.3] cDNA into pLV[Exp]-EGFP-EF1A lentiviral vector (VectorBuilder). Lentivirus carrying GSDMC shRNA sequence (5'-CCTAGAAACTGTTGTGACATTCAAGAGATGTCACAACAGTTTCTAGG-3') (Miguchi, et al., 2016) was constructed on pLV[shRNA]-EGFP-U6 lentiviral backbone (VectorBuilder). All cloned DNA fragments were validated by DNA sequencing. All lentiviruses were produced with a titer of $>10^8$ pfu/ml. To transduce HCT116 cells, lentivirus particles were incubated with HCT116 cell cultures at 10 MOI in the presence of 6 μg/ml polybrene at 37°C. Human or mouse organoid lentiviral transduction was carried out according to a procedure previously described (Maru, et al., 2016) with some modifications. Briefly, the entire contents in the well (organoids, Matrigel and medium) were collected into a 15 ml conical tube using a cell scraper. After centrifugation (5 min at 290 × g), the medium and Matrigel were aspirated carefully. The organoids were then dissociated into single cells by incubating in 1 ml of Accumax solution at 37°C. Enzymes in Accumax were washed out using cold PBS, and single cells were precipitated by centrifugation (5 min at 290 × g). The single-cell pellets were resuspended in the IntestiCult Organoid Growth Medium (StemCell Technologies) supplemented with 2.5 μM CHIR-99021 (APExBIO). Meanwhile, 0.1 ml of cold liquid Matrigel was added into a pre-warmed 48 well plate and incubated at 37°C for 20 min for solidification. Then the single cell or organoid suspension, lentivirus (at 10 MOI) and polybrene (6 μg/ml) were mixed and placed on the solidified Matrigel, and the mixture was incubated at 37°C overnight. Human organoids cultured in IntestiCult Organoid Growth Medium (Human) were directly incubated with lentivirus in the

presence of polybrene. On day 2 (16 h later), the medium with dead cells were removed and another 0.1 ml of ice-cold liquid Matrigel was added to cover the cells. After solidification, IntestiCult Organoid Growth Medium was added to continue the organoid culture. Lentiviral transduction efficiency was estimated by observing GFP expression in the organoids under a fluorescent microscope.

Cell transfection

To silence METTL14 and GSDMC, HCT116 cells were transfected with METTL14 siRNA (Sigma-Aldrich) or GSDMC siRNA2 (Miguchi, et al., 2016) using Lipofectamine 3000. The siRNA sequences were listed in Table S2.

Isolation of colon crypt cells for RNA or protein extraction

Mouse colonic epithelial cells were purified according to previously published methods (Ayyaz, et al., 2019; Hwang, et al., 2018; Atarashi, et al., 2011) with modifications. Freshly collected colons were cut open longitudinally, rinsed with ice-cold PBS, and then cut into 2 mm segments. The segmented tissues were incubated in cold PBS containing 10 mM EDTA at 4°C for 45 min with rotation (45 rpm/min). After centrifugation, the segments were washed with cold PBS once, and then resuspended in 1 ml cold PBS. The suspension was pipetted up and down 40 times using a 1 ml pipettor, and passed through a 70-μm cell strainer to enrich crypts. Then the suspension was resuspended in 5 ml of 20% Percoll and overlaid on 2.5 ml of 40% Percoll in a 15 ml Falcon tube. Percoll gradient separation was performed by centrifugation at 780 x g for 20 min at 25°C. The cells in the interface were collected for RNA or protein extraction.

RT-PCR

Total RNAs were extracted using TRIzol reagent (ThermoFisher). First-strand cDNAs were synthesized using a ReverTra Ace qPCR RT kit (TOYOBO). Real time PCR was carried out in a LightCycler 480 Instrument II real-time PCR system (Roche), using a SYBR Green Realtime PCR Master Mix kit (TOYOBO). The relative amounts of transcripts were calculated using the $2^{-\Delta\Delta Ct}$ formula (Schmittgen and Livak, 2008), normalized to GAPDH transcript as an internal control. PCR primers were listed in Table S2.

Western blotting

Tissue and cell samples were homogenized in Laemmli buffer. Protein concentration was determined using a Bio-Rad DC RC protein assay kit. Protein lysates were separated by SDS-PAGE and then electroblotted onto Immobilon-P membranes. The membranes were blotted with primary antibodies purchased commercially, followed by incubation with horseradish peroxidase-conjugated secondary antibody. Protein bands were visualized using chemiluminescence, using an ECL Western Blot Substrate kit (ThermoFisher). Detailed Western blot procedures were described previously (Li, et al., 2001). Primary antibodies used for Western blot analyses were listed in the Key Resources Table.

m^{6}A quantitation

The ratio of m^{6}A/A in colonic epithelial cells was quantified using the LC-MS/MS method as described previously (Jia, et al., 2011). Briefly, poly(A$^+$) RNAs were purified using a Dynabeads mRNA Purification Kit (ThermoFisher). The poly(A$^+$) RNAs (1 μg) were digested with nuclease P1 (2 U, Wako) at 37°C for 1 hour in 40 μl of buffer, followed by addition of NH_4HCO_3 (1M, 3 μl) and alkaline phosphatase (0.5 U, Sigma). After incubation for additional 1 hour, the samples was diluted 5 times, and 10 μl of the solution was injected into LC-MS/MS for analysis. Nuclosides were separated by reverase phase untra-performance liqid chromatography on a C18 column, with online mass spectrometry detection using Agilent 6410 QQQ triple-quadrupole LC mass spectrometer in positive electrospray ionization mode. The nucleosides were quantified using the nucleoside to base ion mass transitions of 282 to 150 (m^{6}A) and 268 to 136 (A). Nucleoside quantitation was based on the standard curve obtained from pure nucleoside standards running at the same batch of samples. The amount of m^{6}A in total cellular RNAs was also quantified using an EpiQuik m^{6}A RNA Methylation kit (Epigentek) according to the manufacturer's instruction.

scRNA-seq

Mouse colonic epithelial cells were isolated according to previously published methods (Ayyaz, et al., 2019; Parikh, et al., 2019) with some modifications. Briefly, freshly collected colons were cut open longitudinally, rinsed with ice-cold PBS three times, then cut into 2 mm segments. The segmented tissues were incubated in cold PBS containing 10 mM EDTA at 4°C for 45 min with rotation (45 rpm/min). After centrifugation, the segments were collected, washed with cold PBS once, resuspended in 1 ml cold PBS and pipetted up and down 40 times using a 1 ml pipettor. Then the suspension was passed through a 70-μm cell strainer, and the solution that contained epithelial crypts was collected and centrifuged at 4°C for 5 min. The pellet was digested into a single-cell suspension using a Papain Dissociation System (Worthington) according to the manufacturer's instruction. The isolated cells were counted and cell viability was examined using Trypan Blue. Cell preparations with viability >90% were used for scRNA-seq. Colonic epithelial cells pooled from 3 M14$^{f/f}$ mice and 3 IEC-M14$^{-/-}$ mice were subjected to scRNA-seq analysis using the 10x Genomics instruments. CellRanger software v.3.1.0 (Zheng, et al., 2017) developed by 10x Genomics (https://support.10xgenomics.com/single-cell-gene-expression/software/overview/welcome) was used to process raw scRNA-seq sequencing data, where the raw base call (BCL) files of scRNA-seq data were demultiplexed by cellranger mkfastq, followed by mouse reference genome (Ensembl 93) alignment, filtering, barcode and UMI counting via cellranger count with parameter options (--expect-cells=5000, --localmem=120). The filtered feature-barcode matrix with cells presenting at least 200 gene features and each gene feature presented at least in 3 cells was processed with Seurat (Stuart, et al., 2019) for downstream analysis. Doublet cells were detected and cross validated with DoubletDecon (DePasquale, et al., 2019) medoids and centroids methods at the blacklist genes correlation upper cutoff (rpho) of 1. The identified doublet cells and poor quality cells indicated by ≥ 20% mitochondrial content were further removed from downstream analysis. The standard log-normalization was employed to preprocess the count data (scale.factor = 10000). Top 2000 highly variable features were identified with respect to wildtype (M14$^{f/f}$) and mutant (IEC-M14$^{-/-}$) mice separately. Then a harmonized reference was constructed

via an integration process in Seurat (Butler, et al., 2018) from preprocessed count data of wildtype and mutant mice for dimensional reductions, where a linear transformation scaling procedure was applied prior to the PCA dimensional reduction. A graph-based cell clustering approach was performed based on the top principal components determined by the JackStraw procedure (resolution = 0.5). In the end, a tSNE non-linear dimensional reduction method was applied to visualize the clustering results. Identified cell clusters were manually annotated with previous knowledge based on the identified significantly expressed gene markers of each cluster. Up and down regulated gene markers in mutant mice were identified with Wilcox test in Seurat (Stuart, et al., 2019) at FDR correctly p-value of 0.05 and log fold change threshold of 0.25 in comparison with the wildtype mice with respect to each type of annotated cluster cells. The median expression values of selected gene markers on each identified annotated cell clusters and cells with respect to the experimental conditions (wildtype vs mutant) were presented via dot plots and feature plots respectively. Cell cycle was analyzed with Seurat function CellCycleScoring() based on 43 S phase and 54 G2/M phase cell cycle canonical gene markers, and key proliferation markers were visualized with respect to cell cycle phases. The original code of this entire analysis workflow has been deposited at Zenodo (DOI:10.5281/zenodo.6653388).

RNA-seq

Total RNAs were extracted from purified colonic epithelial cells from 3 pairs of $M14^{f/f}$ and IEC-$M14^{-/-}$ mice using TRIzol Reagent (ThermoFisher). Poly(A^+) mRNAs were subsequently purified from 3 μg total RNAs using a Dynabeads mRNA Purification Kit (ThermoFisher) and used for library construction. RNA-seq libraries were prepared using a SMARTer Stranded RNA-Seq Kit (TaKaRa) according to the manufacturer's instruction as reported previously (Du, et al., 2020). The libraries were sequenced using an Illumina HiSeq 4000 System with single end 50-bp reads. Sequencing raw data were preprocessed using trim_galore v0.6.5 with options (--illumina --quality 30 --length 10), and reads were mapped by STAR (Dobin, et al., 2013) v2.6.1d against Gencode GRCm38 (release M25) reference genome with extra options (--readFilesCommand zcat --runThreadN 8 --outSAMtype BAM SortedByCoordinate). The gene level read counts were obtained using FeatureCount v1.6.4. Differential expression was analyzed using R v4.0.2 and edgeR v3.26.5 package. P-values were adjusted for multiple testing using the false discovery rate (FDR) correction of Benjamini and Hochberg (Benjamini and Hochberg, 1995). Significant genes were determined based on an FDR threshold of 5% (0.05). GO (Gene Ontology) biological process enrichment analysis of differentially expressed genes (DEGs) was accomplished using R package clusterProfiler (Yu, et al., 2012) on KEGG (https://www.genome.jp/kegg/) database.

m^6A RIP-seq

Total RNAs were extracted from purified colonic epithelial cells from 3 pairs of $M14^{f/f}$ and IEC-$M14^{-/-}$ mice using TRIzol Reagent (ThermoFisher). Poly(A^+) mRNAs were purified from 20 μg total RNAs using a Dynabeads mRNA Purification Kit (ThermoFisher) and used for m^6A RIP-seq as reported previously (Du, et al., 2020). The poly(A^+) mRNAs were fragmented using RNA Fragmentation Reagents (ThermoFisher). A portion of fragmented mRNAs (4%) was saved as input control. The fragmented RNAs were incubated with

anti-m^{6}A antibody and m^{6}A-IP was performed using an EpiMark N6-Methyladenosine Enrichment Kit (New England Biolabs) following the manufacturer's protocols. The IP-purified mRNA fragments were used to construct libraries using a SMARTer Stranded Total RNA-seq Kit v2-Pico Input Mammalian (TaKaRa) according to the manufacturer's protocol. Sequencing of the libraries was carried out on an Illumina HiSeq 4000 Instrument with single-end 50-bp reads. Sequencing raw data were preprocessed by trim galore v0.6.5 and then mapped against mm10 reference genome by HISAT2 (Kim, et al., 2015) v2.1.0. Peak calling was carried out using R package exomePeak (Meng, et al., 2013). Downstream analysis and visualization of data were accomplished using R v3.6. Identified peaks were annotated via ChIPseeker in R (Yu, et al., 2015). Motif search was performed using HOMER (Heinz, et al., 2010) v4.10.0. The longest isoform was retained if a gene has more than one isoform.

m^{6}A RIP-qPCR

Poly(A$^+$) mRNAs were fragmented using RNA Fragmentation Reagents (ThermoFisher). A portion of fragmented mRNAs was saved as input control. Fragmented mRNAs were incubated with anti-m6A antibody, and antibody-bound mRNA fragments were purified using the EpiMark N6-Methyladenosine Enrichment Kit (New England Biolabs). The IP-purified mRNA fragments were reversed-transcribed into cDNA using hexamer random primer, and short sequences (100-150 bp) covering the m^{6}A sites were quantified by real time PCR. PCR primers are listed in Table S2. The enrichment of m^{6}A was determined by normalization to the input.

GsdmC mRNA decay in organoids

Colonic organoid cultures derived from M14$^{f/f}$ and M14$^{f/f}$;Cdx2-CreERT2 mice were treated with ethanol (EtOH) or 4-hydroxytamoxifen (4-OHT, 200 nM). After 12 hours, actinomycin D at a final concentration of 5 μg/ml was added to the cultures. Cellular RNAs were extracted at 0, 2, 4, and 8 hours following actinomycin D treatment, and *GsdmC* transcripts at each time point were quantified by real time RT-PCR. The mRNA level at each time point was normalized to that at 0 hour, and the changes were plotted against time.

Assessment of Newly translated GsdmC protein in organoids

GsdmC protein synthesis in organoids were assessed by pulse labelling with **L**-azidohomoalanine (AHA, Click Chemistry Tools) as previously reported (Du, et al., 2020). Colonic organoids derived from M14$^{f/f}$ and M14$^{f/f}$;Cdx2-CreERT2 mice were treated with EtOH or 4-OHT (200 nM). After 24 hours, the culture media were replaced with methionine (Met)-free RPMI1640. After 30 min starvation, the media were changed to Met-free RPMI1640 containing 40 μM AHA and incubation was continued for one or two hours. Then the organoids were harvested, washed with PBS and lysed with 1% SDS in 50 mM Tris–HCl (pH 8.0) containing protease inhibitors by sonication for 30 s. After incubation for 30 min on ice lysates were harvested after centrifugation at 12,000 x g for 20 min. Then 200 μg of lysates from each sample were subjected to biotinylation via Click reaction using Biotin-PGE4-Alkyne and a Click & Go Protein Reaction Buffer Kit (Click Chemistry Tools) according to the manufacture's instruction. The reaction was terminated by adding methanol

and chloroform, and proteins were recovered according to a method described previously (Wessel and Flugge, 1984). The recovered protein pellets were air-dried and re-dissolved in RIPA buffer (50 mM Tris–HCl, pH 7.5; 150 mM NaCl; 1% Triton X-100; 0.5% sodium deoxycholate; 0.1% SDS, 1% DTT, and protease inhibitors). After removing unsoluble materials by centrifugation (12,000 x g, 20 min), 1/10 material was saved as inputs, and then streptavidin-coated magnetic beads (High Capacity Streptavidin Magnetic Beads, Click Chemistry Tools) were added to precipitate the AHA-labelled proteins. After incubation for 2 hours at 4°C on a rotator, the beads were harvested on a magnetic stand. The beads were washed with 1% SDS made in PBS and proteins were dissolved in Laemmli buffer. After boiling, the proteins were separated by SDS-PAGE, and the nascent GsdmC proteins were visualized by Western blotting. The inputs were also used for Western blotting to measure total GsdmC, Mettl14 and β-actin.

QUANTIFICATION AND STATISTICAL ANALYSIS

Data values were presented as means ± SD. Most experiments were repeated at least twice. All bioinformatic analyses were conducted using samples of biological triplicates. Statistical analyses were performed using GraphPad Prism Version 9.1.0. For two group comparisons unpaired two-tailed Student's *t*-test was used, and for three or more group comparisons ordinary one-way or two-way analysis of variance (ANOVA) was performed. Animal survival rates were estimated by the Kaplan-Meier method and groups were analyzed by the log-rank test. P values < 0.05 were considered statistically significant.

Supplementary Material

Refer to Web version on PubMed Central for supplementary material.

Acknowledgements

This work was supported by National Institutes of Health grants R21AI140152, R01AI151162, RM1HG008935 and 5UL1TR002389, Kenneth Rainin Foundation grant 2019-1137, and the Duchossois Family Institute at the University of Chicago. C.H. is an Howard Hughes Medical Institute Investigator. We thank Alex Gregorieff (McGill University) for providing Clu-CreERT2 transgenic mice.

REFERENCES

Alarcon CR, Goodarzi H, Lee H, Liu X, Tavazoie S, and Tavazoie SF (2015). HNRNPA2B1 Is a Mediator of m(6)A-Dependent Nuclear RNA Processing Events. Cell 162, 1299–308. [PubMed: 26321680]

Atarashi K, Tanoue T, Shima T, Imaoka A, Kuwahara T, Momose Y, Cheng G, Yamasaki S, Saito T, Ohba Y, et al. (2011). Induction of colonic regulatory T cells by indigenous Clostridium species. Science 331, 337–41. [PubMed: 21205640]

Ayyaz A, Kumar S, Sangiorgi B, Ghoshal B, Gosio J, Ouladan S, Fink M, Barutcu S, Trcka D, Shen J, et al. (2019). Single-cell transcriptomes of the regenerating intestine reveal a revival stem cell. Nature 569, 121–125. [PubMed: 31019301]

Barker N, van Es JH, Kuipers J, Kujala P, van den Born M, Cozijnsen M, Haegebarth A, Korving J, Begthel H, Peters PJ, et al. (2007). Identification of stem cells in small intestine and colon by marker gene Lgr5. Nature 449, 1003–7. [PubMed: 17934449]

Batista PJ, Molinie B, Wang J, Qu K, Zhang J, Li L, Bouley DM, Lujan E, Haddad B, Daneshvar K, et al. (2014). m(6)A RNA modification controls cell fate transition in mammalian embryonic stem cells. Cell Stem Cell 15, 707–19. [PubMed: 25456834]

Benjamini Y, and Hochberg Y (1995). Controlling the False Discovery Rate - a Practical and Powerful Approach to Multiple Testing. J R Stat Soc B 57, 289–300.

Broz P, Pelegrin P, and Shao F (2020). The gasdermins, a protein family executing cell death and inflammation. Nat Rev Immunol 20, 143–157. [PubMed: 31690840]

Butler A, Hoffman P, Smibert P, Papalexi E, and Satija R (2018). Integrating single-cell transcriptomic data across different conditions, technologies, and species. Nat Biotechnol 36, 411–420. [PubMed: 29608179]

Chen T, Hao YJ, Zhang Y, Li MM, Wang M, Han W, Wu Y, Lv Y, Hao J, Wang L, et al. (2015). m(6)A RNA methylation is regulated by microRNAs and promotes reprogramming to pluripotency. Cell Stem Cell 16, 289–301. [PubMed: 25683224]

Cui Q, Shi H, Ye P, Li L, Qu Q, Sun G, Sun G, Lu Z, Huang Y, Yang CG, et al. (2017). m6A RNA Methylation Regulates the Self-Renewal and Tumorigenesis of Glioblastoma Stem Cells. Cell Rep 18, 2622–2634. [PubMed: 28297667]

DePasquale EAK, Schnell DJ, Van Camp PJ, Valiente-Alandi I, Blaxall BC, Grimes HL, Singh H, and Salomonis N (2019). DoubletDecon: Deconvoluting Doublets from Single-Cell RNA-Sequencing Data. Cell Rep 29, 1718–1727 e8. [PubMed: 31693907]

Ding J, Wang K, Liu W, She Y, Sun Q, Shi J, Sun H, Wang DC, and Shao F (2016). Pore-forming activity and structural autoinhibition of the gasdermin family. Nature 535, 111–6. [PubMed: 27281216]

Dobin A, Davis CA, Schlesinger F, Drenkow J, Zaleski C, Jha S, Batut P, Chaisson M, and Gingeras TR (2013). STAR: ultrafast universal RNA-seq aligner. Bioinformatics 29, 15–21. [PubMed: 23104886]

Dominissini D, Moshitch-Moshkovitz S, Schwartz S, Salmon-Divon M, Ungar L, Osenberg S, Cesarkas K, Jacob-Hirsch J, Amariglio N, Kupiec M, et al. (2012). Topology of the human and mouse m6A RNA methylomes revealed by m6A-seq. Nature 485, 201–6. [PubMed: 22575960]

Du H, Zhao Y, He J, Zhang Y, Xi H, Liu M, Ma J, and Wu L (2016). YTHDF2 destabilizes m(6)A-containing RNA through direct recruitment of the CCR4-NOT deadenylase complex. Nat Commun 7, 12626. [PubMed: 27558897]

Du J, Chen Y, Shi Y, Liu T, Cao Y, Tang Y, Ge X, Nie H, Zheng C, and Li YC (2015). 1,25-Dihydroxyvitamin D Protects Intestinal Epithelial Barrier by Regulating the Myosin Light Chain Kinase Signaling Pathway. Inflamm Bowel Dis 21, 2495–506. [PubMed: 26287999]

Du J, Liao W, Liu W, Deb DK, He L, Hsu PJ, Nguyen T, Zhang L, Bissonnette M, He C, et al. (2020). N(6)-Adenosine Methylation of Socs1 mRNA Is Required to Sustain the Negative Feedback Control of Macrophage Activation. Dev Cell 55, 737–753 e7. [PubMed: 33220174]

Du J, Wei X, Ge X, Chen Y, and Li YC (2017). Microbiota-Dependent Induction of Colonic Cyp27b1 Is Associated With Colonic Inflammation: Implications of Locally Produced 1,25-Dihydroxyvitamin D3 in Inflammatory Regulation in the Colon. Endocrinology 158, 4064–4075. [PubMed: 28938443]

Feng S, Fox D, and Man SM (2018). Mechanisms of Gasdermin Family Members in Inflammasome Signaling and Cell Death. J Mol Biol 430, 3068–3080. [PubMed: 29990470]

Frye M, Harada BT, Behm M, and He C (2018). RNA modifications modulate gene expression during development. Science 361, 1346–1349. [PubMed: 30262497]

Geula S, Moshitch-Moshkovitz S, Dominissini D, Mansour AA, Kol N, Salmon-Divon M, Hershkovitz V, Peer E, Mor N, Manor YS, et al. (2015). Stem cells. m6A mRNA methylation facilitates resolution of naive pluripotency toward differentiation. Science 347, 1002–6. [PubMed: 25569111]

Gregorieff A, and Clevers H (2005). Wnt signaling in the intestinal epithelium: from endoderm to cancer. Genes Dev 19, 877–90. [PubMed: 15833914]

Han B, Yan S, Wei S, Xiang J, Liu K, Chen Z, Bai R, Sheng J, Xu Z, and Gao X (2020). YTHDF1-mediated translation amplifies Wnt-driven intestinal stemness. EMBO Rep 21, e49229. [PubMed: 32064749]

He L, Zhou M, and Li YC (2019). Vitamin D/Vitamin D Receptor Signaling Is Required for Normal Development and Function of Group 3 Innate Lymphoid Cells in the Gut. iScience 17, 119–131. [PubMed: 31272068]

Heinz S, Benner C, Spann N, Bertolino E, Lin YC, Laslo P, Cheng JX, Murre C, Singh H, and Glass CK (2010). Simple combinations of lineage-determining transcription factors prime cis-regulatory elements required for macrophage and B cell identities. Mol Cell 38, 576–89. [PubMed: 20513432]

Hinoi T, Akyol A, Theisen BK, Ferguson DO, Greenson JK, Williams BO, Cho KR, and Fearon ER (2007). Mouse model of colonic adenoma-carcinoma progression based on somatic Apc inactivation. Cancer Res 67, 9721–30. [PubMed: 17942902]

Hou J, Zhao R, Xia W, Chang CW, You Y, Hsu JM, Nie L, Chen Y, Wang YC, Liu C, et al. (2020). PD-L1-mediated gasdermin C expression switches apoptosis to pyroptosis in cancer cells and facilitates tumour necrosis. Nat Cell Biol 22, 1264–1275. [PubMed: 32929201]

Huang H, Weng H, and Chen J (2020). The Biogenesis and Precise Control of RNA m(6)A Methylation. Trends Genet 36, 44–52. [PubMed: 31810533]

Huang H, Weng H, Sun W, Qin X, Shi H, Wu H, Zhao BS, Mesquita A, Liu C, Yuan CL, et al. (2018). Recognition of RNA N(6)-methyladenosine by IGF2BP proteins enhances mRNA stability and translation. Nat Cell Biol 20, 285–295. [PubMed: 29476152]

Hwang B, Lee JH, and Bang D (2018). Single-cell RNA sequencing technologies and bioinformatics pipelines. Exp Mol Med 50, 96.

Jia G, Fu Y, Zhao X, Dai Q, Zheng G, Yang Y, Yi C, Lindahl T, Pan T, Yang YG, et al. (2011). N6-methyladenosine in nuclear RNA is a major substrate of the obesity-associated FTO. Nat Chem Biol 7, 885–7. [PubMed: 22002720]

Johansson ME, Sjovall H, and Hansson GC (2013). The gastrointestinal mucus system in health and disease. Nat Rev Gastroenterol Hepatol 10, 352–61. [PubMed: 23478383]

Kayagaki N, Stowe IB, Lee BL, O'Rourke K, Anderson K, Warming S, Cuellar T, Haley B, Roose-Girma M, Phung QT, et al. (2015). Caspase-11 cleaves gasdermin D for non-canonical inflammasome signalling. Nature 526, 666–71. [PubMed: 26375259]

Kim D, Langmead B, and Salzberg SL (2015). HISAT: a fast spliced aligner with low memory requirements. Nat Methods 12, 357–60. [PubMed: 25751142]

Koranda JL, Dore L, Shi H, Patel MJ, Vaasjo LO, Rao MN, Chen K, Lu Z, Yi Y, Chi W, et al. (2018). Mettl14 Is Essential for Epitranscriptomic Regulation of Striatal Function and Learning. Neuron 99, 283–292 e5. [PubMed: 30056831]

Kretzschmar K, and Clevers H (2016). Organoids: Modeling Development and the Stem Cell Niche in a Dish. Dev Cell 38, 590–600. [PubMed: 27676432]

Laukoetter MG, Bruewer M, and Nusrat A (2006). Regulation of the intestinal epithelial barrier by the apical junctional complex. Curr Opin Gastroenterol 22, 85–9. [PubMed: 16462161]

Lee H, Bao S, Qian Y, Geula S, Leslie J, Zhang C, Hanna JH, and Ding L (2019). Stage-specific requirement for Mettl3-dependent m(6)A mRNA methylation during haematopoietic stem cell differentiation. Nat Cell Biol 21, 700–709. [PubMed: 31061465]

Li HB, Tong J, Zhu S, Batista PJ, Duffy EE, Zhao J, Bailis W, Cao G, Kroehling L, Chen Y, et al. (2017). m6A mRNA methylation controls T cell homeostasis by targeting the IL-7/STAT5/SOCS pathways. Nature 548, 338–342. [PubMed: 28792938]

Li YC, Bolt MJG, Cao L-P, and Sitrin MD (2001). Effects of vitamin D receptor inactivation on the expression of calbindins and calcium metabolism. Am J Physiol Endocrinol Metab 281, E558–E564. [PubMed: 11500311]

Liu J, Yue Y, Han D, Wang X, Fu Y, Zhang L, Jia G, Yu M, Lu Z, Deng X, et al. (2014). A METTL3-METTL14 complex mediates mammalian nuclear RNA N6-adenosine methylation. Nat Chem Biol 10, 93–5. [PubMed: 24316715]

Liu X, Zhang Z, Ruan J, Pan Y, Magupalli VG, Wu H, and Lieberman J (2016). Inflammasome-activated gasdermin D causes pyroptosis by forming membrane pores. Nature 535, 153–8. [PubMed: 27383986]

Madison BB, Dunbar L, Qiao XT, Braunstein K, Braunstein E, and Gumucio DL (2002). Cis elements of the villin gene control expression in restricted domains of the vertical (crypt) and horizontal (duodenum, cecum) axes of the intestine. J Biol Chem 277, 33275–83. [PubMed: 12065599]

Maru Y, Orihashi K, and Hippo Y (2016). Lentivirus-Based Stable Gene Delivery into Intestinal Organoids. Methods Mol Biol 1422, 13–21. [PubMed: 27246018]

Meng J, Cui X, Rao MK, Chen Y, and Huang Y (2013). Exome-based analysis for RNA epigenome sequencing data. Bioinformatics 29, 1565–7. [PubMed: 23589649]

Miguchi M, Hinoi T, Shimomura M, Adachi T, Saito Y, Niitsu H, Kochi M, Sada H, Sotomaru Y, Ikenoue T, et al. (2016). Gasdermin C Is Upregulated by Inactivation of Transforming Growth Factor beta Receptor Type II in the Presence of Mutated Apc, Promoting Colorectal Cancer Proliferation. PLoS One 11, e0166422. [PubMed: 27835699]

Mukherji A, Kobiita A, Ye T, and Chambon P (2013). Homeostasis in Intestinal Epithelium Is Orchestrated by the Circadian Clock and Microbiota Cues Transduced by TLRs. Cell 153, 812–27. [PubMed: 23663780]

Narayan P, and Rottman FM (1988). An in vitro system for accurate methylation of internal adenosine residues in messenger RNA. Science 242, 1159–62. [PubMed: 3187541]

Noah TK, Donahue B, and Shroyer NF (2011). Intestinal development and differentiation. Exp Cell Res 317, 2702–10. [PubMed: 21978911]

Noah TK, and Shroyer NF (2013). Notch in the intestine: regulation of homeostasis and pathogenesis. Annu Rev Physiol 75, 263–88. [PubMed: 23190077]

Parikh K, Antanaviciute A, Fawkner-Corbett D, Jagielowicz M, Aulicino A, Lagerholm C, Davis S, Kinchen J, Chen HH, Alham NK, et al. (2019). Colonic epithelial cell diversity in health and inflammatory bowel disease. Nature 567, 49–55. [PubMed: 30814735]

Park CM, Reid PE, Walker DC, and MacPherson BR (1987). A simple, practical 'swiss roll' method of preparing tissues for paraffin or methacrylate embedding. J Microsc 145 (Pt 1), 115–20. [PubMed: 2437310]

Perochon J, Carroll LR, and Cordero JB (2018). Wnt Signalling in Intestinal Stem Cells: Lessons from Mice and Flies. Genes (Basel) 9.

Ping XL, Sun BF, Wang L, Xiao W, Yang X, Wang WJ, Adhikari S, Shi Y, Lv Y, Chen YS, et al. (2014). Mammalian WTAP is a regulatory subunit of the RNA N6-methyladenosine methyltransferase. Cell Res 24, 177–89. [PubMed: 24407421]

Qiu W, Wu B, Wang X, Buchanan ME, Regueiro MD, Hartman DJ, Schoen RE, Yu J, and Zhang L (2011). PUMA-mediated intestinal epithelial apoptosis contributes to ulcerative colitis in humans and mice. J Clin Invest 121, 1722–32. [PubMed: 21490394]

R Core Team (2020). R: A language and environment for statistical computing. R Foundation for Statistical Computing, Vienna, Austria. URL https://www.R-project.org/.

Rakoff-Nahoum S, Paglino J, Eslami-Varzaneh F, Edberg S, and Medzhitov R (2004). Recognition of commensal microflora by toll-like receptors is required for intestinal homeostasis. Cell 118, 229–41. [PubMed: 15260992]

Rana N, Privitera G, Kondolf HC, Bulek K, Lechuga S, De Salvo C, Corridoni D, Antanaviciute A, Maywald RL, Hurtado AM, et al. (2022). GSDMB is increased in IBD and regulates epithelial restitution/repair independent of pyroptosis. Cell 185, 283–298 e17. [PubMed: 35021065]

Rath HC, Herfarth HH, Ikeda JS, Grenther WB, Hamm TE Jr., Balish E, Taurog JD, Hammer RE, Wilson KH, and Sartor RB (1996). Normal luminal bacteria, especially Bacteroides species, mediate chronic colitis, gastritis, and arthritis in HLA-B27/human beta2 microglobulin transgenic rats. J Clin Invest 98, 945–53. [PubMed: 8770866]

Riedl SJ, and Salvesen GS (2007). The apoptosome: signalling platform of cell death. Nat Rev Mol Cell Biol 8, 405–13. [PubMed: 17377525]

Sancho R, Cremona CA, and Behrens A (2015). Stem cell and progenitor fate in the mammalian intestine: Notch and lateral inhibition in homeostasis and disease. EMBO Rep 16, 571–81. [PubMed: 25855643]

Sangiorgi E, and Capecchi MR (2008). Bmi1 is expressed in vivo in intestinal stem cells. Nat Genet 40, 915–20. [PubMed: 18536716]

Santos AJM, Lo YH, Mah AT, and Kuo CJ (2018). The Intestinal Stem Cell Niche: Homeostasis and Adaptations. Trends Cell Biol 28, 1062–1078. [PubMed: 30195922]

Schmittgen TD, and Livak KJ (2008). Analyzing real-time PCR data by the comparative C(T) method. Nat Protoc 3, 1101–8. [PubMed: 18546601]

Shi H, Wang X, Lu Z, Zhao BS, Ma H, Hsu PJ, Liu C, and He C (2017). YTHDF3 facilitates translation and decay of N6-methyladenosine-modified RNA. Cell Res 27, 315–328. [PubMed: 28106072]

Shi H, Zhang X, Weng YL, Lu Z, Liu Y, Lu Z, Li J, Hao P, Zhang Y, Zhang F, et al. (2018). m(6)A facilitates hippocampus-dependent learning and memory through YTHDF1. Nature 563, 249–253. [PubMed: 30401835]

Shi J, Zhao Y, Wang K, Shi X, Wang Y, Huang H, Zhuang Y, Cai T, Wang F, and Shao F (2015). Cleavage of GSDMD by inflammatory caspases determines pyroptotic cell death. Nature 526, 660–5. [PubMed: 26375003]

Shirihai OS, Song M, and Dorn GW 2nd (2015). How mitochondrial dynamism orchestrates mitophagy. Circ Res 116, 1835–49. [PubMed: 25999423]

Stuart T, Butler A, Hoffman P, Hafemeister C, Papalexi E, Mauck WM 3rd, Hao Y, Stoeckius M, Smibert P, and Satija R (2019). Comprehensive Integration of Single-Cell Data. Cell 177, 1888–1902 e21. [PubMed: 31178118]

Su L, Nalle SC, Shen L, Turner ES, Singh G, Breskin LA, Khramtsova EA, Khramtsova G, Tsai PY, Fu YX, et al. (2013). TNFR2 activates MLCK-dependent tight junction dysregulation to cause apoptosis-mediated barrier loss and experimental colitis. Gastroenterology 145, 407–15. [PubMed: 23619146]

Tait SW, and Green DR (2013). Mitochondrial regulation of cell death. Cold Spring Harb Perspect Biol 5.

Takeda N, Jain R, LeBoeuf MR, Wang Q, Lu MM, and Epstein JA (2011). Interconversion between intestinal stem cell populations in distinct niches. Science 334, 1420–4. [PubMed: 22075725]

Tamura M, Tanaka S, Fujii T, Aoki A, Komiyama H, Ezawa K, Sumiyama K, Sagai T, and Shiroishi T (2007). Members of a novel gene family, Gsdm, are expressed exclusively in the epithelium of the skin and gastrointestinal tract in a highly tissue-specific manner. Genomics 89, 618–29. [PubMed: 17350798]

Van der Sluis M, De Koning BA, De Bruijn AC, Velcich A, Meijerink JP, Van Goudoever JB, Buller HA, Dekker J, Van Seuningen I, Renes IB, et al. (2006). Muc2-deficient mice spontaneously develop colitis, indicating that MUC2 is critical for colonic protection. Gastroenterology 131, 117–29. [PubMed: 16831596]

Wang Q, Wang Y, Ding J, Wang C, Zhou X, Gao W, Huang H, Shao F, and Liu Z (2020a). A bioorthogonal system reveals antitumour immune function of pyroptosis. Nature 579, 421–426. [PubMed: 32188939]

Wang R, Li H, Wu J, Cai ZY, Li B, Ni H, Qiu X, Chen H, Liu W, Yang ZH, et al. (2020b). Gut stem cell necroptosis by genome instability triggers bowel inflammation. Nature 580, 386–390. [PubMed: 32296174]

Wang X, Lu Z, Gomez A, Hon GC, Yue Y, Han D, Fu Y, Parisien M, Dai Q, Jia G, et al. (2014a). N6-methyladenosine-dependent regulation of messenger RNA stability. Nature 505, 117–20. [PubMed: 24284625]

Wang Y, Chiang IL, Ohara TE, Fujii S, Cheng J, Muegge BD, Ver Heul A, Han ND, Lu Q, Xiong S, et al. (2019). Long-Term Culture Captures Injury-Repair Cycles of Colonic Stem Cells. Cell 179, 1144–1159 e15. [PubMed: 31708126]

Wang Y, Li Y, Toth JI, Petroski MD, Zhang Z, and Zhao JC (2014b). N6-methyladenosine modification destabilizes developmental regulators in embryonic stem cells. Nat Cell Biol 16, 191–8. [PubMed: 24394384]

Watson AJ, Chu S, Sieck L, Gerasimenko O, Bullen T, Campbell F, McKenna M, Rose T, and Montrose MH (2005). Epithelial barrier function in vivo is sustained despite gaps in epithelial layers. Gastroenterology 129, 902–12. [PubMed: 16143130]

Weng H, Huang H, Wu H, Qin X, Zhao BS, Dong L, Shi H, Skibbe J, Shen C, Hu C, et al. (2018). METTL14 Inhibits Hematopoietic Stem/Progenitor Differentiation and Promotes Leukemogenesis via mRNA m(6)A Modification. Cell Stem Cell 22, 191–205 e9. [PubMed: 29290617]

Wessel D, and Flugge UI (1984). A method for the quantitative recovery of protein in dilute solution in the presence of detergents and lipids. Anal Biochem 138, 141–3. [PubMed: 6731838]

Yan KS, Chia LA, Li X, Ootani A, Su J, Lee JY, Su N, Luo Y, Heilshorn SC, Amieva MR, et al. (2012). The intestinal stem cell markers Bmi1 and Lgr5 identify two functionally distinct populations. Proceedings of the National Academy of Sciences of the United States of America 109, 466–71. [PubMed: 22190486]

Yu G, Wang LG, Han Y, and He QY (2012). clusterProfiler: an R package for comparing biological themes among gene clusters. OMICS 16, 284–7. [PubMed: 22455463]

Yu G, Wang LG, and He QY (2015). ChIPseeker: an R/Bioconductor package for ChIP peak annotation, comparison and visualization. Bioinformatics 31,2382–3. [PubMed: 25765347]

Zaccara S, Ries RJ, and Jaffrey SR (2019). Reading, writing and erasing mRNA methylation. Nat Rev Mol Cell Biol 20, 608–624. [PubMed: 31520073]

Zhan M, Brooks C, Liu F, Sun L, and Dong Z (2013). Mitochondrial dynamics: regulatory mechanisms and emerging role in renal pathophysiology. Kidney international 83, 568–81. [PubMed: 23325082]

Zhang S, Zhao BS, Zhou A, Lin K, Zheng S, Lu Z, Chen Y, Sulman EP, Xie K, Bogler O, et al. (2017). m6A Demethylase ALKBH5 Maintains Tumorigenicity of Glioblastoma Stem-like Cells by Sustaining FOXM1 Expression and Cell Proliferation Program. Cancer Cell 31, 591–606 e6. [PubMed: 28344040]

Zhang Z, Zhang Y, Xia S, Kong Q, Li S, Liu X, Junqueira C, Meza-Sosa KF, Mok TMY, Ansara J, et al. (2020). Gasdermin E suppresses tumour growth by activating anti-tumour immunity. Nature 579, 415–420. [PubMed: 32188940]

Zhao BS, Roundtree IA, and He C (2017). Post-transcriptional gene regulation by mRNA modifications. Nat Rev Mol Cell Biol 18, 31–42. [PubMed: 27808276]

Zheng G, Dahl JA, Niu Y, Fedorcsak P, Huang CM, Li CJ, Vagbo CB, Shi Y, Wang WL, Song SH, et al. (2013). ALKBH5 is a mammalian RNA demethylase that impacts RNA metabolism and mouse fertility. Mol Cell 49, 18–29. [PubMed: 23177736]

Zheng GX, Terry JM, Belgrader P, Ryvkin P, Bent ZW, Wilson R, Ziraldo SB, Wheeler TD, McDermott GP, Zhu J, et al. (2017). Massively parallel digital transcriptional profiling of single cells. Nat Commun 8, 14049. [PubMed: 28091601]

Zhou Z, He H, Wang K, Shi X, Wang Y, Su Y, Wang Y, Li D, Liu W, Zhang Y, et al. (2020). Granzyme A from cytotoxic lymphocytes cleaves GSDMB to trigger pyroptosis in target cells. Science 368.

Highlights

- Colonic epithelial m^{6}A depletion leads to colitis, growth retardation and premature death
- m^{6}A depletion induces excess apoptosis that disrupts colonic mucosal morphogenesis
- m^{6}A depletion triggers *GsdmC* degradation leading to mitochondrial dysfunction
- *GsdmC* m^{6}A is required for Lgr5$^+$ stem cell survival to maintain colonic homeostasis

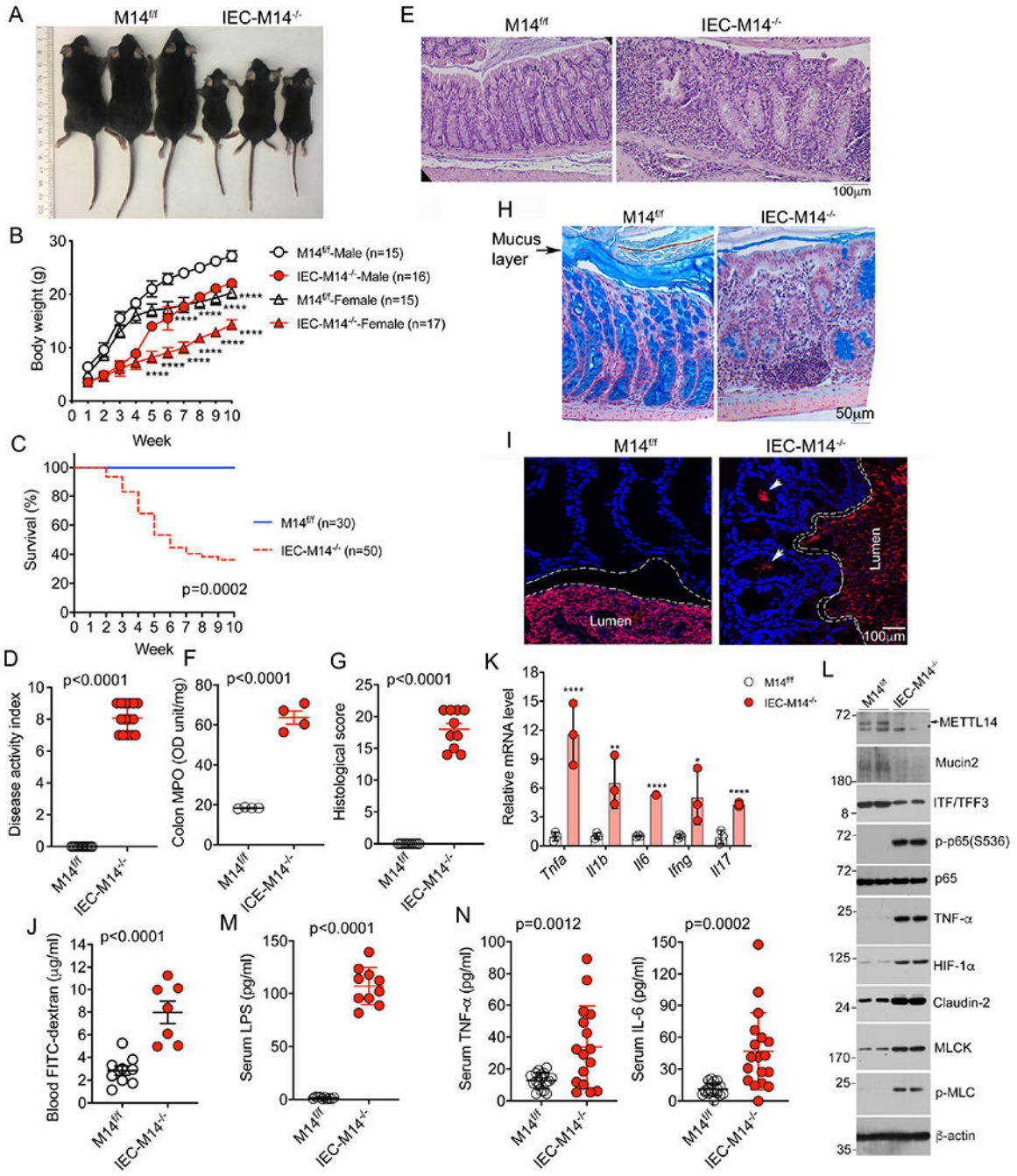

Figure 1. Gut epithelial *Mettl14* deletion leads to spontaneous inflammation, severe growth retardation and pre-mature death due to disruption of normal colonic epithelial morphogenesis.

(A) Gross appearance of $M14^{f/f}$ and IEC-$M14^{-/-}$ mice at approximately 5 weeks of age;

(B) Growth curves of male and female mice within 10 weeks after birth; ****p<0.0001 vs. corresponding $M14^{f/f}$, by Student's t test;

(C) Kaplan-Meier survival curves;

(D) Disease activity index, n=15 each group;

(E) H&E staining of colon sections from 3-month old mice;

(F) Colon mucosal myeloperoxidase (MPO) activity; n=4 each group;

(G) Colon section histological scores; n=10 each group;
(H) Alcian blue staining of colon sections fixed *en masse* with luminal contents. *Arrow* indicates the mucus layer;
(I) Fluorescent *in situ* hybridization (FISH) with 16S rRNA probe on colon sections; Space between luminal bacteria and epithelial surface are marked by *dash lines*; *Arrows* indicate invaded bacteria within the lamina propria in IEC-M14$^{-/-}$ colon;
(J) Blood FITC-dextran concentrations measured at 2.5 hours after FITC-dextran gavage; n=8-9 each group;
(K) RT-qPCR quantitation of pro-inflammatory cytokines in colonic mucosa; *p<0.05; **p<0.01; ****p<0.0001 vs. corresponding M14$^{f/f}$, by two-way ANOVA;
(L) Western blot analyses of purified colonic crypt lysates;
(M) Serum LPS levels; n=10 each group;
(N) Serum TNF-α and IL-6 concentrations; n=12-18 each group. All data are presented as mean ± SD.
See also Figures S1, S2, S3.

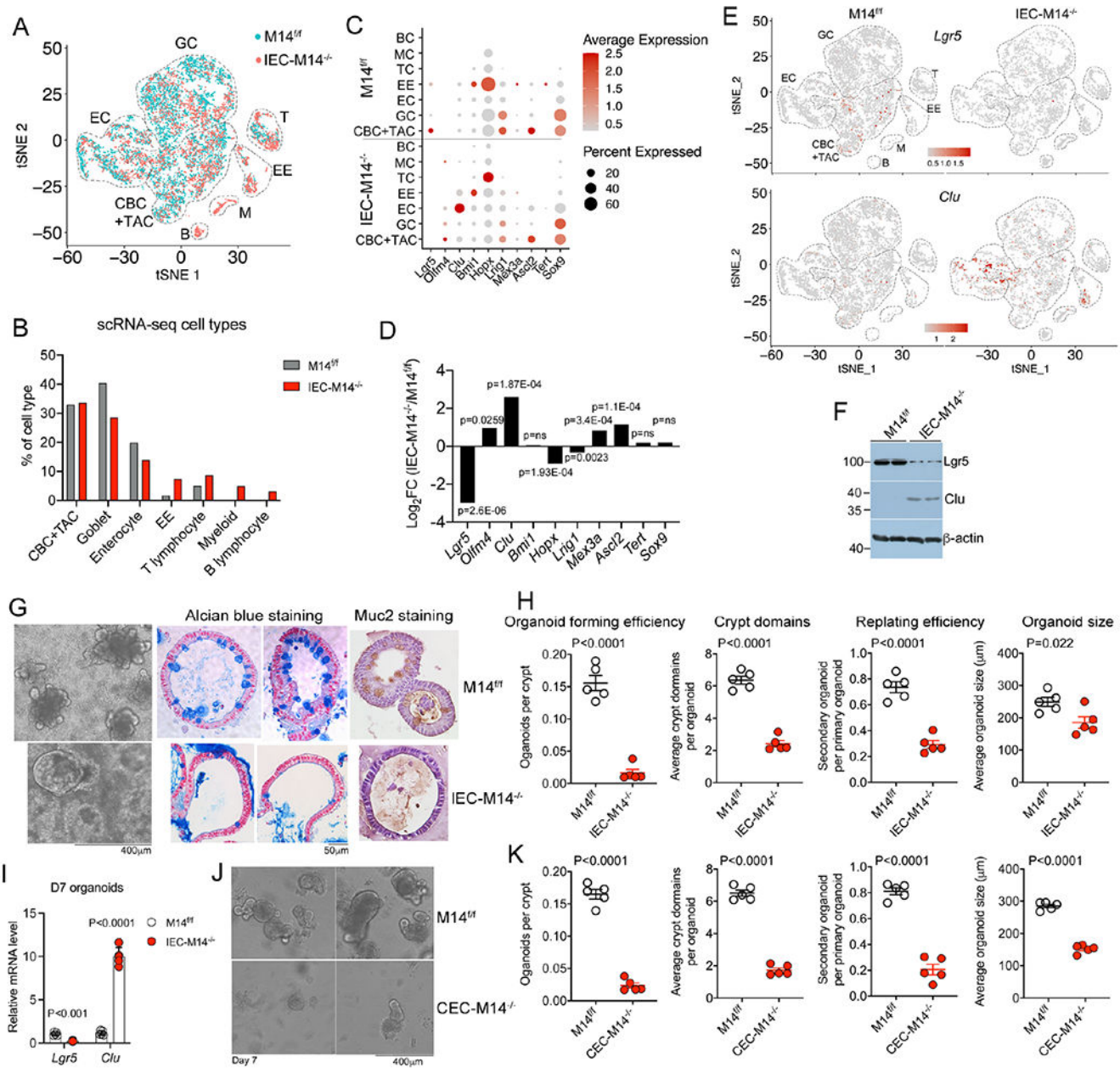

Figure 2. Mettl14 depletion impairs intestinal stem cells.

(A) Overlapped maps of t-distributed stochastic neighbour embedding (t-SNE) clusters of colonic crypt cells from M14$^{f/f}$ and IEC-M14$^{-/-}$ mice. Clusters are grouped based on known cell-specific markers. CBC: Crypt base columnar cell; TAC: Transit amplifying cell; GC: Goblet cell; EC: Enterocyte; EE: Enteroendocrine cell; T: T lymphocyte; M: Myeloid cell; B: B lymphocyte.

(B) Quantitation (%) of cell populations identified in the colonic crypts of M14$^{f/f}$ and IEC-M14$^{-/-}$ mice;

(C) Dot plots showing ISC marker distributions in M14$^{f/f}$ and IEC-M14$^{-/-}$ cell populations;

(D) RNA-seq data showing the log fold changes in ISC marker gene expression between $M14^{f/f}$ and IEC-$M14^{-/-}$ colons;
(E) Feature plots showing the cell populations expressing *Lgr5* or *Clu* in $M14^{f/f}$ and IEC-$M14^{-/-}$ mice;
(F) Western blot analysis of Lgr5 and Clu protein in purified $M14^{f/f}$ and IEC-$M14^{-/-}$ colonic crypts;
(G) Images of day 7 colonic organoids (*left panels*), and organoid sections stained with Alcian blue (*middle panels*) or anti-Muc2 antibody (*right panels*) from $M14^{f/f}$ and IEC-$M14^{-/-}$ mice;
(H) Quantitation of organoid forming efficiency, crypt domains per organoid, organoid replating efficiency and organoid size in colonic organoids derived from $M14^{f/f}$ and IEC-$M14^{-/-}$ mice;
(I) RT-qPCR quantitation of *Lgr5* and *Clu* transcripts in $M14^{f/f}$ and IEC-$M14^{-/-}$ organoids on day 7;
(J) Images of day 7 colonic organoids from $M14^{f/f}$ and CEC-$M14^{-/-}$ mice;
(K) Quantitation of organoid forming efficiency, crypt domains per organoid, organoid replating efficiency and organoid size in colonic organoids from $M14^{f/f}$ and CEC-$M14^{-/-}$ mice. Crypt domains and organoid size are determined by counting 50 organoids per mice for each data point. Data are presented as mean ± SD. See also Figures S4, S5.

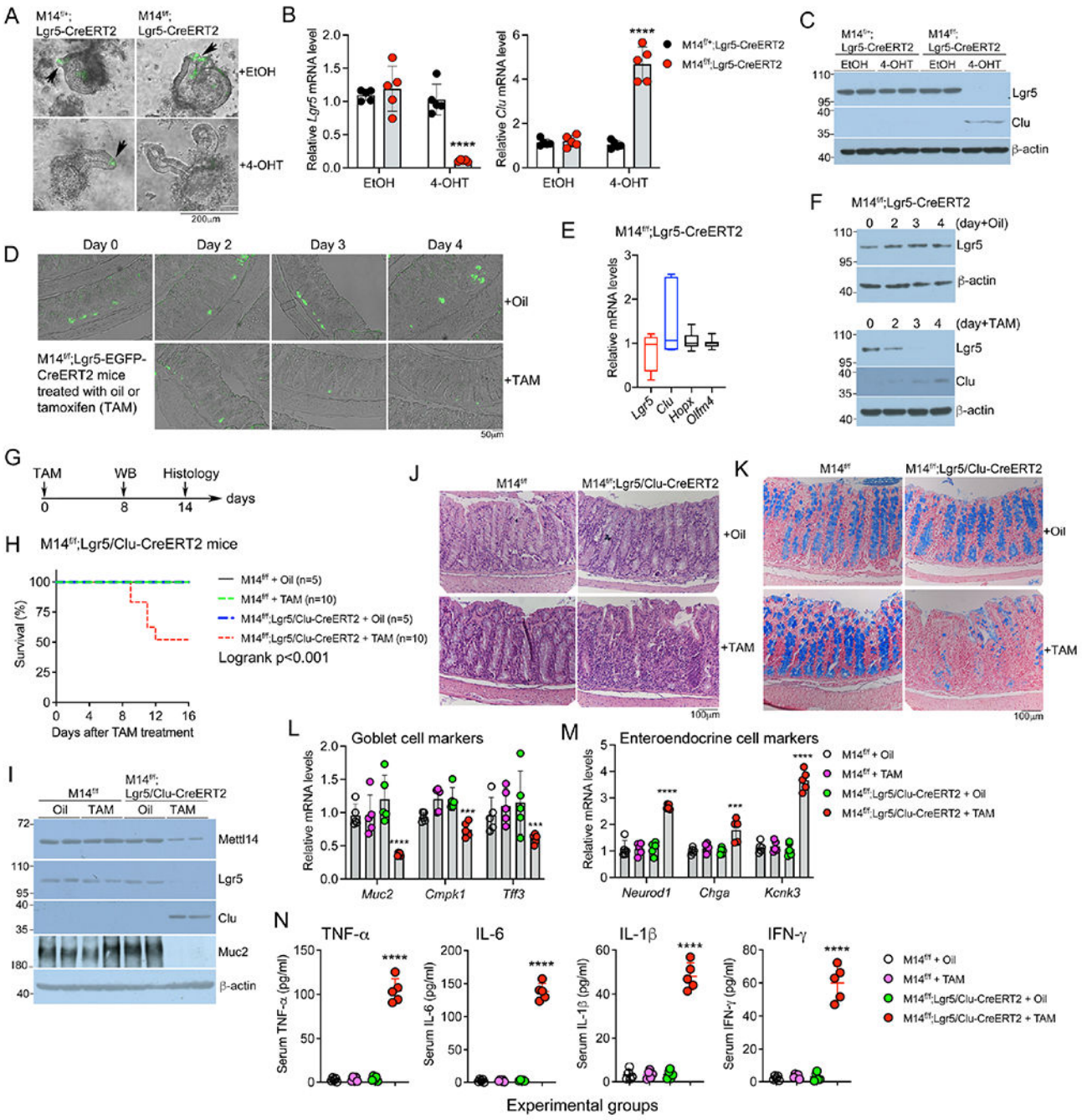

Figure 3. Simultaneous depletion of Mettl14 from Lgr5^{+} and Clu^{+} cells disrupts normal colonic mucosal morphogenesis.

(A) Colonic organoids derived from M14$^{f/+}$;Lgr5-EGFP-CreERT2 and M14$^{f/f}$;Lgr5-EGFP-CreERT2 mice, on day 4 after being treated with ethanol (EtOH) or 4-hydroxytamoxifen (4-OHT); *Arrows* indicate GFP^{+}(Lgr5^{+}) cells;

(B) RT-qPCR quantitation of *Lgr5* and *Clu* transcripts in M14$^{f/+}$;Lgr5-CreERT2 and M14$^{f/f}$;Lgr5-CreERT2 organoids treated with EtOH or 4-OHT for 4 days; **** p<0.0001 vs. the rest, by two-way ANOVA;

(C) Western blotting analyses confirm elimination of Lgr5 protein and induction of Clu protein in $M14^{f/f}$;Lgr5-CreERT2 organoids 4 days after 4-OHT treatment;
(D) Daily changes (0-4 days) of GFP^+ ($Lgr5^+$) ISCs in $M14^{f/f}$;Lgr5-CreERT2 mice treated with Oil vehicle or tamoxifen (TAM). Note TAM treatment eliminates GFP^+ ($Lgr5^+$) cells at the crypt base within 3-4 days;
(E) RT-qPCR quantification of changes in *Lgr5*, *Clu*, *Hopx* and *Olfm4* transcripts in $M14^{f/f}$;Lgr5-CreERT2 colonic crypts on day 4 following TAM treatment;
(F) Time course changes of Lgr5 and Clu proteins in purified $M14^{f/f}$;Lgr5-CreERT2 colonic crypts from $M14^{f/f}$;Lgr5-CreERT2 mice following Oil or TAM treatment. Note Lgr5 loss is accompanied by Clu induction;
(G) Schematic illustration of experimental design for $M14^{f/f}$;Lgr5/Clu-CreERT2 mice;
(H) Kaplan-Meier survival curves of $M14^{f/f}$ and $M14^{f/f}$;Lgr5/Clu-CreERT2 mice following oil or TAM treatment;
(I) Western blot analyses of purified colonic crypts from $M14^{f/f}$ and $M14^{f/f}$;Lgr5/Clu-CreERT2 mice on day 8 after oil or TAM treatment;
(J, K) H&E (J) and Alcian blue (K) staining of colon sections from $M14^{f/f}$ and $M14^{f/f}$;Lgr5/Clu-CreERT2 mice on day 14 after Oil or TAM treatment;
(L,M) RT-qPCR quantitation of goblet cell markers (L) and enteroendocrine cell markers (M) in purified colonic crypts on day 14 following Oil or TAM treatment;
(N) Serum cytokine concentrations determined on day 14 after Oil or TAM treatment;
**** $p<0.0001$ vs. the rest, by two-way ANOVA; Data are presented as mean ± SD. See also Figure S6.

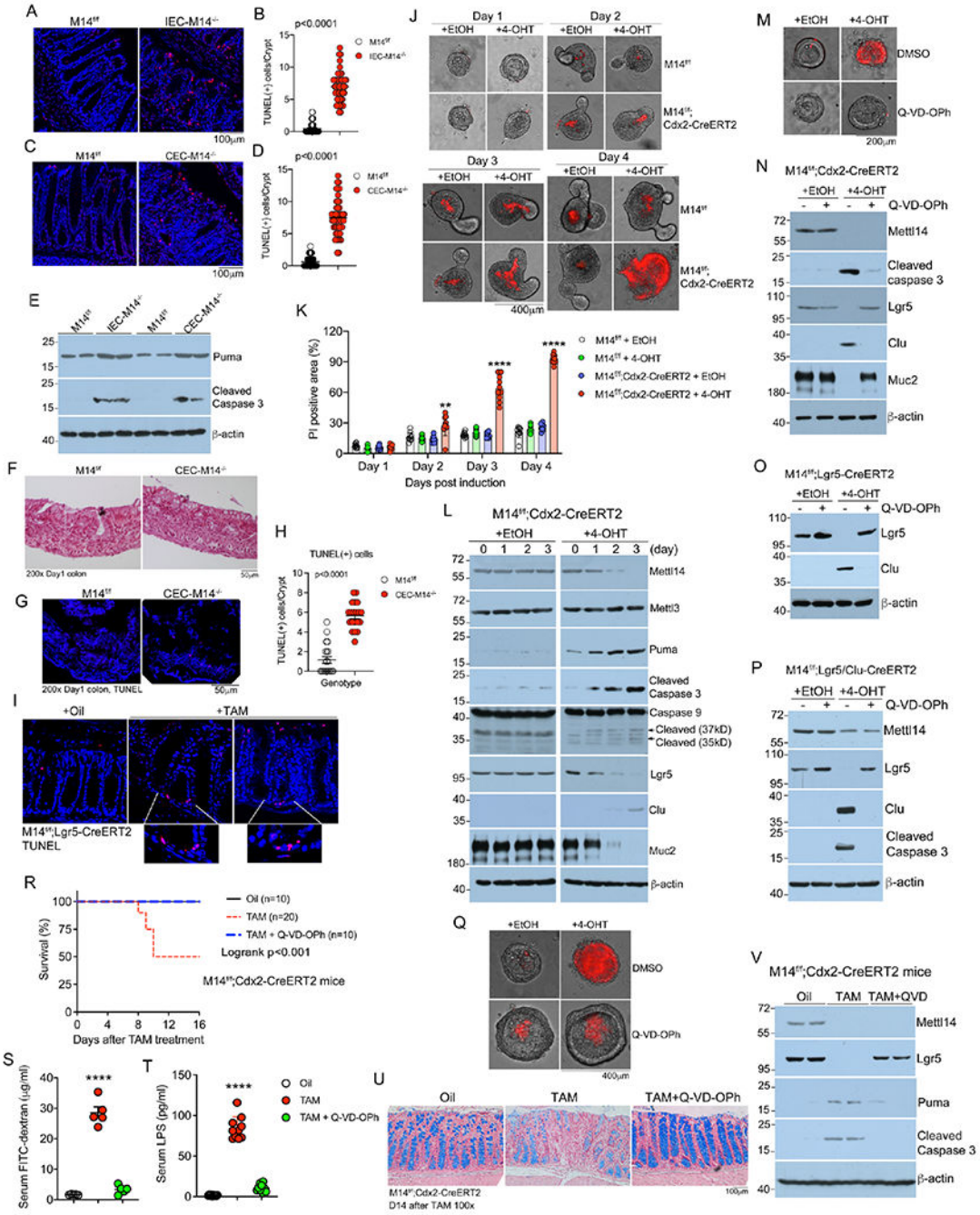

Figure 4. Mettl14 depletion triggers excess apoptosis that impairs colon mucosal morphogenesis.

(A-D) TUNEL staining (A,C) and quantitation of TUNEL-positive cells (B,D) of $M14^{f/f}$ and IEC-$M14^{-/-}$ colon sections (A,B) or $M14^{f/f}$ and CEC-$M14^{-/-}$ colon sections (C,D);

(E) Western blot analysis of Puma and activated caspase 3 in purified $M14^{f/f}$, IEC-$M14^{-/-}$ and CEC-$M14^{-/-}$ colon crypts;

(F-H) H&E staining (F), TUNEL staining (G) and TUNEL-positive cell quantitation (H) of colon sections from one-day old $M14^{f/f}$ and CEC-$M14^{-/-}$ mice;

(I) TUNEL staining of colon sections from $M14^{f/f}$;Lgr5-CreERT2 mice on day 3 following Oil or TAM treatment. The *lower panels* are enlarged images of the indicated crypt base;
(J,K) Time-dependent changes of propidium iodide (PI)-stained $M14^{f/f}$ and $M14^{f/f}$;Cdx2-CreERT2 colonic organoids on day 1 through day 4 following treatment with EtOH or 4-OHT (J) and quantitation of PI-positive area (K); **p<0.01; ****p<0.0001 vs. the rest within the group, by two-way ANOVA;
(L) Western blot analyses of time-dependent changes in $M14^{f/f}$;Cdx2-CreERT2 organoids treated with EtOH or 4-OHT for 0 to 3 days;
(M) PI-staining of $M14^{f/f}$;Cdx2-CreERT2 organoids treated with EtOH or 4-OHT in the presence of DMSO or Q-VD-OPh for 4 days;
(N-P) Western blot analyses of $M14^{f/f}$;Cdx2-CreERT2 organoids (N), $M14^{f/f}$;Lgr5-CreERT2 organoids (O) or $M14^{f/f}$;Lgr5/Clu-CreERT2 organoids (P) treated with EtOH or 4-OHT in the presence of DMSO or Q-VD-OPh for 3 days;
(Q) PI-staining of $M14^{f/f}$;Lgr5/Clu-CreERT2 organoids treated with EtOH or 4-OHT in the presence of DMSO or Q-VD-OPh for 4 days;
(R) Kaplan-Meier survival curves of adult $M14^{f/f}$;Cdx2-CreERT2 mice after being treated with Oil, TAM or TAM+Q-VD-OPh;
(S) Serum FITC-dextran concentrations measured at 2.5 hours after FITC-dextran gavage of $M14^{f/f}$;Cdx2-CreERT2 mice on day 14 following treatment with Oil, TAM or TAM+Q-VD-OPh;
****p<0.0001 vs. the rest, by two-way ANOVA;
(T) Serum LPS concentrations in $M14^{f/f}$;Cdx2-CreERT2 mice on day 14 after treatment with Oil, TAM or TAM+Q-VD-OPh; ****p<0.0001 vs. the rest, by two-way ANOVA. All data are presented as mean ± SD.
(U) Alcian blue staining of colon sections from $M14^{f/f}$;Cdx2-CreERT2 mice on day 14 following treatment with Oil, TAM or TAM+Q-VD-OPh;
(V) Western blot analyses of colon crypt lysates from $M14^{f/f}$;Cdx2-CreERT2 mice on day 14 after treatment with Oil, TAM or TAM+Q-VD-OPh (QVD).

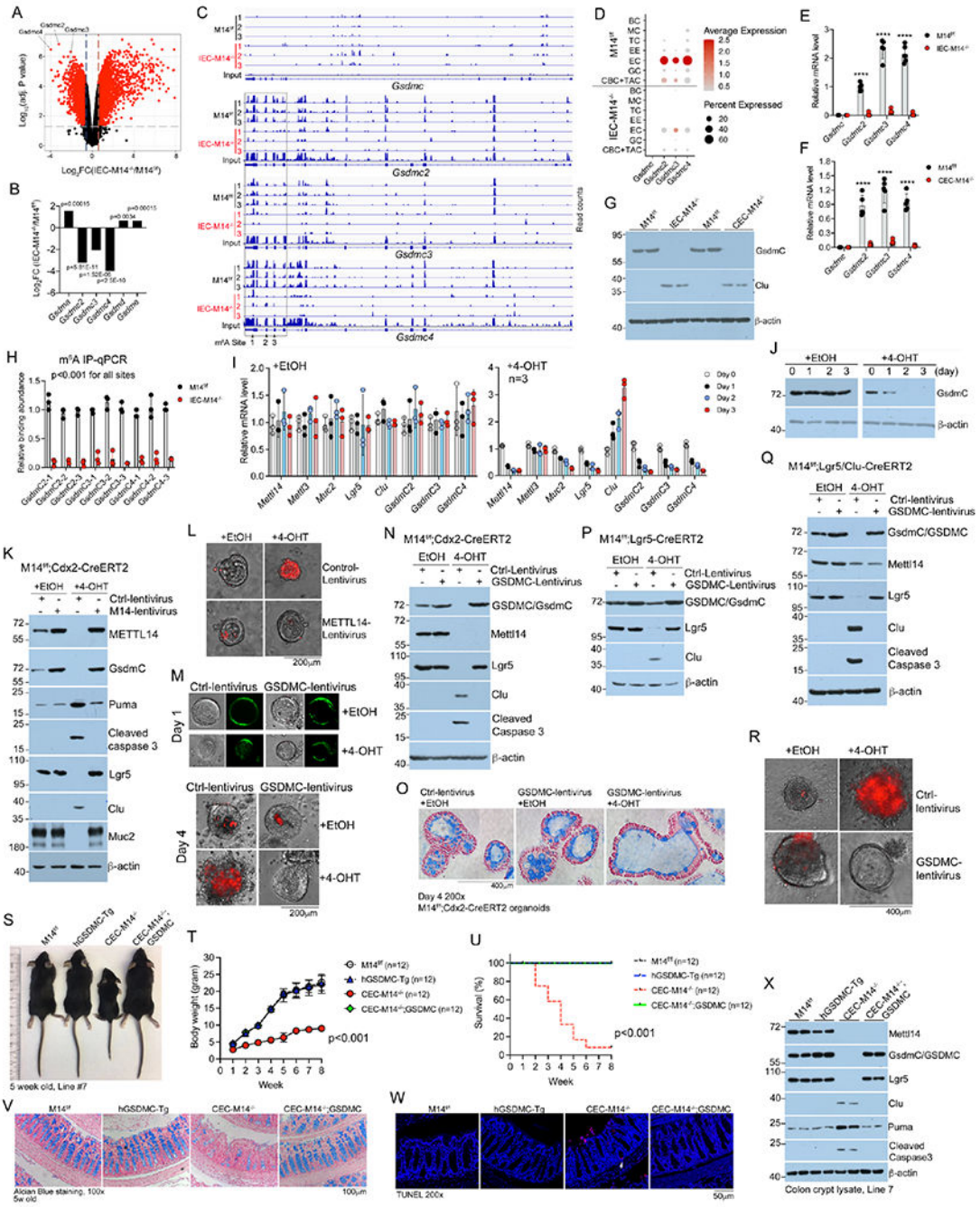

Figure 5. *GsdmC* transcripts are direct targets of Mettl14 to regulate apoptosis.

(A) RNA-seq volcano plots showing the locations of *GsdmC2/3/4* transcripts;

(B) RNA-seq data showing the fold changes of Gsdm family members in $M14^{f/f}$ and IEC-$M14^{-/-}$ colonic crypt cells;

(C) RIP-seq tracks showing read density in *GsdmC1/2/3/4* transcripts in $M14^{f/f}$ and IEC-$M14^{-/-}$ colonic crypt cells. The 3' exons of *GsdmC2/3/4* are *boxed*, and the methylation sites (1,2,3) that were validated by m^6A IP-qPCR in (H) are indicated by *arrow heads*.

(D) scRNA-seq dot plots showing expression of *GsdmC1/2/3/4* transcripts in colonic cell populations of $M14^{f/f}$ and IEC-$M14^{-/-}$ mice;
(E,F) RT-qPCR quantitation of *GsdmC1/2/3/4* transcripts in purified $M14^{f/f}$ and IEC-$M14^{-/-}$ colonic crypt cells (E) or $M14^{f/f}$ and CEC-$M14^{-/-}$ colonic crypt cells (F);
(G) Western blot analysis of GsdmC and Clu protein levels in purified $M14^{f/f}$, IEC-$M14^{-/-}$ and CEC-$M14^{-/-}$ colon crypt cells. Note GsdmC2/3/4 proteins are shown as a single band;
(H) RIP-qPCR quantitation of m^6A at the 3' exon sites (1,2,3 indicated in C) of *GsdmC2/3/4* transcripts in $M14^{f/f}$ and IEC-$M14^{-/-}$ mice;
(I) RT-qPCR quantitation of time course changes of indicated transcripts in $M14^{f/f}$;Cdx2-CreERT2 colonic organoids treated with EtOH or 4-OHT for 0, 1, 2 or 3 days; ***P<0.001 by two-way ANOVA;
(J) Time-dependent changes of GsdmC proteins in $M14^{f/f}$;Cdx2-CreERT2 colonic organoids following EtOH or 4-OHT treatment for 0-3 days. GsdmC2/3/4 proteins are shown as a single band;
(K) Western blot analysis of $M14^{f/f}$;Cdx2-CreERT2 colonic organoids transduced with Ctrl-lentivirus or METTL14-lentivirus on day 3 following EtOH or 4-OHT treatment;
(L) PI-staining of $M14^{f/f}$;Cdx2-CreERT2 colonic organoids transduced with Ctrl-lentivirus or METTL14-lentivirus on day 4 following EtOH or 4-OHT treatment;
(M) PI-staining and GFP expression of $M14^{f/f}$;Cdx2-CreERT2 colonic organoids transduced with Ctrl-lentivirus or GSDMC-lentivirus on days 1 and 4 following EtOH or 4-OHT treatment;
(N) Western blot analysis of $M14^{f/f}$;Cdx2-CreERT2 colonic organoids transduced with Ctrl-lentivirus or GSDMC-lentivirus on day 3 following EtOH or 4-OHT treatment;
(O) Alcian blue staining of Ctrl-lentivirus or GSDMC-lentivirus transduced $M14^{f/f}$;Cdx2-CreERT2 organoid sections on day 4 following EtOH or 4-OHT treatment;
(P,Q) Western blot analysis of $M14^{f/f}$;Lgr5-CreERT2 organoids (P) or $M14^{f/f}$;Lgr5/Clu-CreERT2 organoids
(Q) transduced with Ctrl-lentivirus or GSDMC-lentivirus on day 3 following EtOH or 4-OHT treatment;
(R) PI-staining of $M14^{f/f}$;Lgr5/Clu-CreERT2 organoids transduced with Ctrl-lentivirus or GSDMC-lentivirus on day 4 following EtOH or 4-OHT treatment.
(S) $M14^{f/f}$, hGSDMC-Tg, CEC-$M14^{-/-}$ and CEC-$M14^{-/-}$;GSDMC mice at 5 weeks of age, showing rescue of CEC-$M14^{-/-}$ mice by the GSDMC transgene from Tg line 7.
(T) Growth curves of four genotypes of mice;
(U) Kaplan-Meier survival curves of four genotypes;
(V) Alcian blue staining of colon sections from four genotypes;
(W) TUNEL staining of colon sections from four genotypes. *Arrow* indicates stem cell apoptosis;
(X) Western blot analyses of isolated colonic crypt cells from these four genotypes.
See also Figure S7.

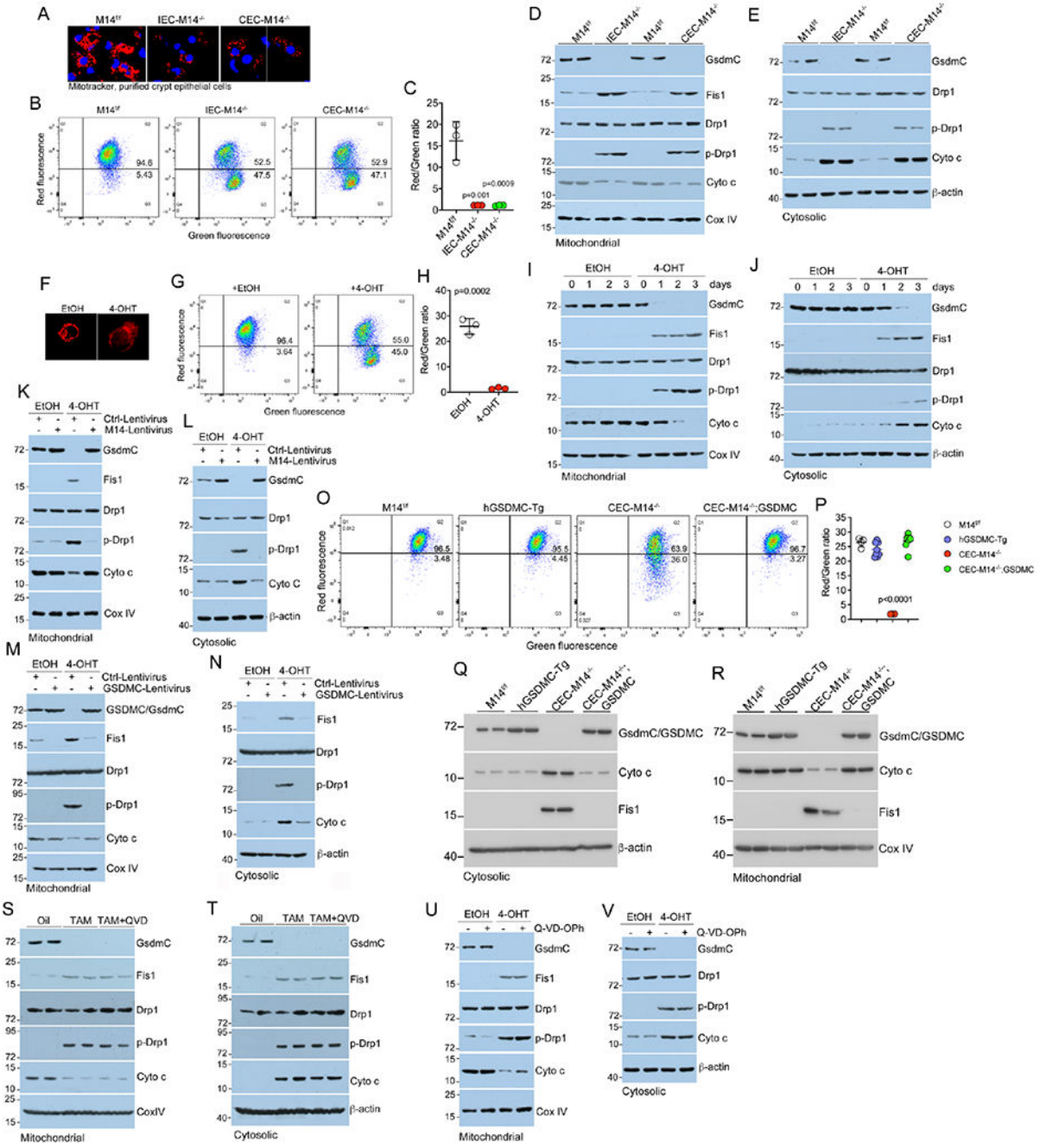

Figure 6. GsdmC is required to maintain mitochondrial membrane potential and structural integrity.

(A) M14$^{f/f}$, IEC-M14$^{-/-}$ and CEC-M14$^{-/-}$ colon crypt cells stained with MitoTracker red dye;

(B) FACS analysis of JC-1 stained M14$^{f/f}$, IEC-M14$^{-/-}$ and CEC-M14$^{-/-}$ colon crypt cells;

(C) Mitochondrial membrane potentials in these cells expressed as Red (Q2) to Green (Q3) ratio based on the FACS data;

(D,E) Western blot analyses of mitochondrial (D) and cytosolic (E) fractions of colon crypt cells purified from M14$^{f/f}$, IEC-M14$^{-/-}$ and CEC-M14$^{-/-}$ mice;

(F) MitoTracker dye staining of $M14^{f/f}$;Cdx2-CreERT2 colonic organoids on day 4 following EtOH or 4-OHT treatment;
(G) FACS analysis of JC-1 stained $M14^{f/f}$;Cdx2-CreERT2 colonic organoids on day 3 following EtOH or 4-OHT treatment;
(H) Mitochondrial membrane potentials in $M14^{f/f}$;Cdx2-CreERT2 colonic organoids on day 3 following EtOH or 4-OHT treatment, expressed as Red (Q2) to Green (Q3) ratio based on the FACS data;
(I,J) Western blot analyses of mitochondrial (I) and cytosolic (J) fractions of $M14^{f/f}$;Cdx2-CreERT2 colonic organoids from day 0 to 3 following EtOH or 4-OHT treatment;
(K,L) Western blot analyses of mitochondrial (K) and cytosolic (L) fractions of $M14^{f/f}$;Cdx2-CreERT2 colonic organoids transduced with Ctrl-lentivirus or METTL14-lentivirus on day 3 following EtOH or 4-OHT treatment;
(M,N) Western blot analyses of mitochondrial (M) and cytosolic (N) fractions of $M14^{f/f}$;Cdx2-CreERT2 organoids transduced with Ctrl-lentivirus or GSDMC-lentivirus on day 3 following EtOH or 4-OHT treatment;
(O) FACS analysis of JC-1 stained colonic crypt cells from $M14^{f/f}$, hGSDMC-Tg, CEC-$M14^{-/-}$ and CEC-$M14^{-/-}$;GSDMC mice at 5 weeks of age;
(P) Mitochondrial membrane potentials in colonic epithelial cells from the four genotypes of mice, expressed as Red (Q2) to Green (Q3) ratio based on the FACS data;
(Q,R) Western blot analyses of cytosolic (Q) and mitochondrial (R) fractions of colonic crypt cells from the four genotypes of mice;
(S,T) Western blot analysis of mitochondrial (S) and cytosolic (T) fractions of purified colonic crypt cells from $M14^{f/f}$;Cdx2-CreERT2 mice treated with oil, TAM or TAM+Q-VD-OPh (QVD) for 14 days;
(U,V) Western blot analyses of mitochondrial (U) and cytosolic (V) fractions of $M14^{f/f}$;Cdx2-CreERT2 organoids on day 3 following EtOH or 4-OHT treatment in the presence or absence of Q-VD-OPh.

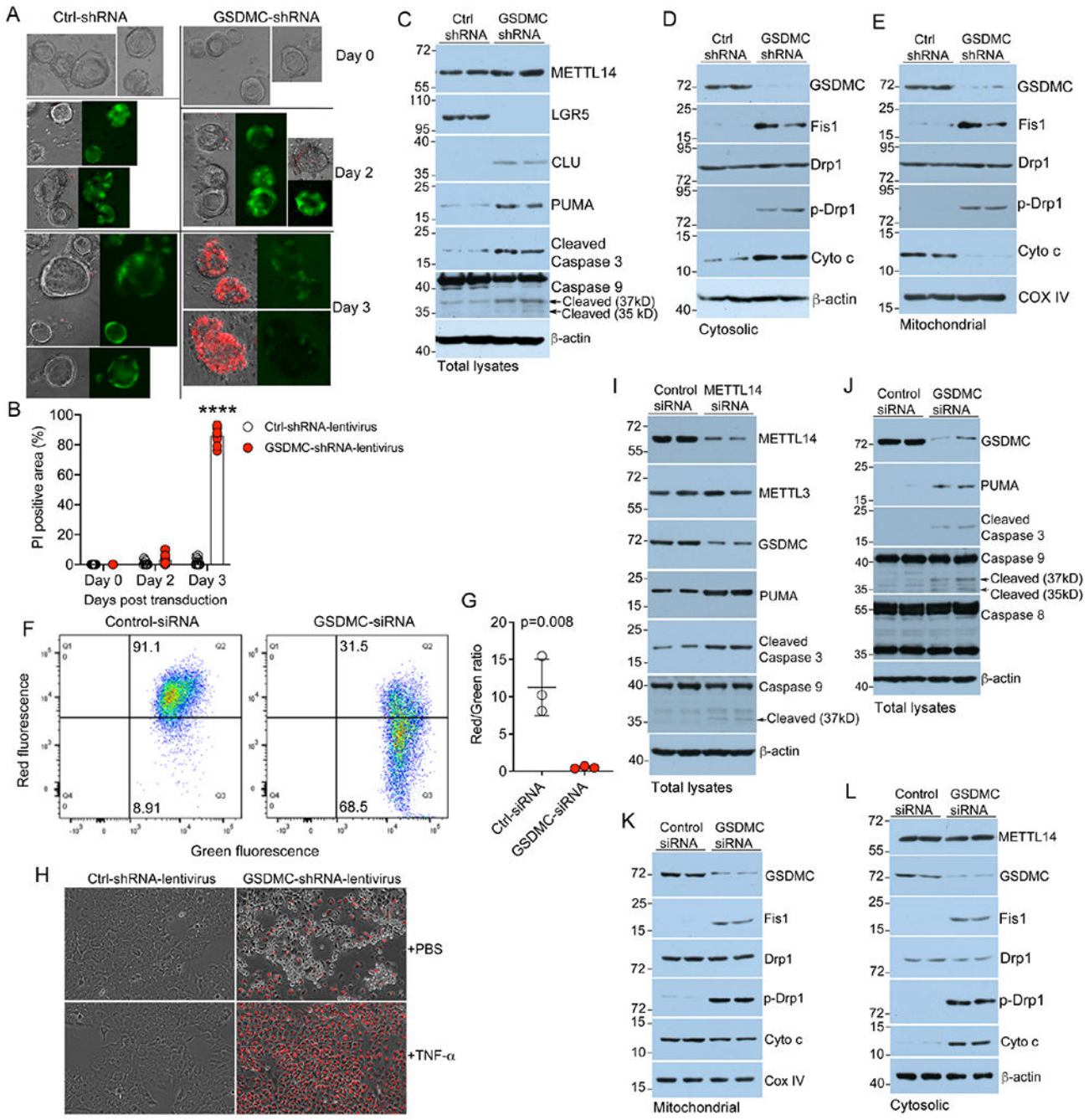

Figure 7. GSDMC knockdown triggers apoptosis in human colonic organoids and colon cancer cells.

(A) PI-staining of human colonic organoids transduced with lentivirus carrying Ctrl-shRNA or GSDMC-shRNA at day 0, 2 and 3 post transduction;

(B) Quantitation of PI-positive area in the organoids; ****p<0.0001 vs. the rest, by two-way ANOVA;

(C) Western blot analyses of total lysates from human colonic organoids transduced with Ctrl-shRNA or GSDMC-shRNA on day 3 post transduction;

(D,E) Western blot analyses of cytosolic fraction (D) or mitochondrial fraction (E) of human colonic organoids transduced with Ctrl-shRNA or GSDMC-shRNA on day 3 post transduction;
(F) FACS analysis of JC-1 stained HCT116 cells transfected with Ctrl-siRNA or GSDMC-siRNA;
(G) Mitochondrial membrane potentials in Ctrl-siRNA- or GSDMC-siRNA-transfected HCT116 cells expressed as Red (Q2) to Green (Q3) ratio based on the FACS data;
(H) PI-staining of HCT116 cells transduced with lentivirus carrying Ctrl-shRNA or GSDMC-shRNA, following by PBS or TNF-α treatment for 24 hours;
(I,J) Western blot analyses of total lysates from HCT116 cells transfected with Ctrl-siRNA or METTL14-siRNA (I) or with Ctrl-siRNA or GSDMC-siRNA (J);
(K,L) Western blot analyses of mitochondrial fraction (K) or cytosolic fraction (L) of HCT116 cells transfected with Ctrl-siRNA or GSDMC-siRNA.

KEY RESOURCES TABLE

Reagent or Resource	Source	Identifier
Antibodies		
Anti-β-actin	Santa Cruz Biotechnology	Cat#: sc-47778, RRID: AB_2714189
Anti-mouse IgG-HRP	Santa Cruz Biotechnology	Cat#: sc-516102, RRID: AB_2687626
Anti-rabbit IgG-HRP	Santa Cruz Biotechnology	Cat#: sc-2357, RRID: AB_628497
Anti-ITF	Santa Cruz Biotechnology	Cat#: sc-398651, RRID: N/A
Anti-TNFα	Santa Cruz Biotechnology	Cat# sc-52746, RRID: AB_630341
Anti-Caspase 9	ProteinTech	Cat#: 10380-1-AP, RRID: AB_2068632
Anti-Caspase 8	ProteinTech	Cat#: 13423-1-AP, RRID: AB_2068463
Anti-GSDMC	ProteinTech	Cat#: 27630-1-AP, RRID: AB_2880930
Anti-CD45	ProteinTech	Cat#: 20103-1-AP, RRID: AB_2716813
Anti-COXIV	ProteinTech	Cat#: 11242-1-AP, RRID: AB_2085278
Anti-Cytochrome C	ProteinTech	Cat#: 66264-1-Ig, RRID: AB_2716798
Anti-FIS1	ProteinTech	Cat#: 10956-1-AP, RRID: AB_2102532
Anti-Clusterin	ProteinTech	Cat#: 12289-1-AP, RRID: AB_2083316
Anti-CD3	Abcam	Cat#: ab16669, RRID: AB_443425
Anti-LGR5	Abcam	Cat#: ab75732, RRID: AB_1310281
Anti-claudin-2	Abcam	Cat# ab76032, RRID: AB_1523364
Anti-MLCK	Abcam	Cat# ab76092, RRID: AB_1524000
Anti-p-mlc	Cell Signaling Technology	Cat# 3674, RRID: AB_2147464
Anti-p65	Cell Signaling Technology	Cat# 8242, RRID: AB_10859369
Anti-p-p65(S536)	Cell Signaling Technology	Cat# 3033, RRID: AB_331284
Anti-Drp1	Cell Signaling Technology	Cat#: 5391S, RRID: AB_11178938
Anti-Phospho-Drp1	Cell Signaling Technology	Cat#: 4494S, RRID: AB_11178659
Anti-Cleaved Caspase 3	Cell Signaling Technology	Cat#: 9664S, RRID: AB_2070042
Anti-PUMA	Cell Signaling Technology	Cat#: 4976S, RRID: AB_2064551
Anti-PUMA	Cell Signaling Technology	Cat#: 7467S, RRID: AB_10829605
Anti-HIF-1α	Millipore	Cat#: Cat# MAB5382, RRID: AB_177967
Anti-Ki67	Novus Biologicals	Cat#: NB110-89717, RRID: AB_1217074
Anti-MUC2	Novus Biologicals	Cat#: NBP1-31231, RRID: AB_10003763
Anti-m6A	Synaptic Systems	Cat#: 202003, RRID: AB_2279214
Anti-METTL14	Sigma-Aldrich	Cat#: HPA038002, RRID: AB_10672401
Anti-METTL3	Aviva Systems Biology	Cat#: ARP39390_T100, RRID: AB_2142045
Chemicals, Peptides and Recombinant Proteins		
Q-VD-OPH	MedKoo Biosciences	Cat#: 526845
Actinomycin D	Sigma-Aldrich	Cat#: A9415
4-Hydroxytamoxifen	Sigma-Aldrich	Cat#: H7904
Tamoxifen	Sigma-Aldrich	Cat#: T5648

Reagent or Resource	Source	Identifier
hMETTL14-siRNA	Sigma-Aldrich	Cat#: EHU038041
hGSDMC-siRNA	Sigma-Aldrich	Cat#: EHU012491
Accumax solution	Sigma-Aldrich	Cat#: A7089
L-Azidohomoalanine	Click Chemistry Tools	Cat#: 1066-25
Biotin-PEG4-Alkyne	Click Chemistry Tools	Cat#: TA105-5
Matrigel Matrix	Corning	Cat#: 356231
CHIR-99021	APExBIO	Cat#: A3011
Propidium iodide	Alfa Aesar	Cat#: J66584
Critical Commercial Assays		
MitoTracker Kit	Cell Signaling	Cat#: 9082
Alcian Blue Kit	Vector Laboratories	Cat#: H-3501
In Situ Cell Death Detection Kit	Roche	Cat#: 12156792910
SYBR Green Realtime PCR Master Mix Kit	TOYOBO	Cat#: QPK-201
ReverTra Ace qPCR RT Kit	TOYOBO	Cat#: FSQ-101
IntestiCult™ Organoid Growth Medium (Mouse)	StemCell Technologies	Cat#: 06005
IntestiCult™ Organoid Growth Medium (Human)	StemCell Technologies	Cat#: 06010
Papain Dissociation System	Worthington	Cat#: LK003150
LPS ELISA Kit	LifeSpan BioSciences	Cat#: LS-F17912
Mitochondria Isolation Kit	ThermoFisher	Cat#: 89801
Dynabeads mRNA Purification kit	ThermoFisher	Cat#: 61006
RPMI1640, no methionine	ThermoFisher	Cat#: A1451701
RNA Fragmentation Reagents	ThermoFisher	Cat#: AM8740
MitoProbe JC-1 Assay Kit	ThermoFisher	Cat#:M34152
SMARTer Stranded RNA-Seq Kit	TaKaRa	Cat#: 634836
SMARTer Stranded RNA-Seq Kit v2-Pico Input Mammalian	TaKaRa	Cat#: 634411
N6-Methyladenosine Enrichment Kit	New England Biolabs	Cat#: E1610S
Magnetic protein G beads	New England Biolabs	Cat#: S1430S
EpiQuik m6A RNA Methylation Quantification Kit	EPIGENTEK	Cat#: P-9005-48
Mouse IL-1β ELISA Kit	BioLegend	Cat#: 432604
Mouse IFN-γ ELISA Kit	BioLegend	Cat#: 430804
Mouse IL-6 ELISA Kit	BioLegend	Cat#: 431304
Mouse TNF-α ELISA Kit	BioLegend	Cat#: 430904
Protein Reaction Buffer Kit	Click Chemistry Tools	Cat#: 1262
Streptavidin Magnetic Beads	Click Chemistry Tools	Cat#:1497-1
Deposited Data		
RNA-seq (Raw and analyzed data)	This study	GEO: GSE181927
m6ARIP-seq (Raw and analyzed data)	This study	GEO: GSE181863
scRNA-seq (Raw and analyzed data)	This study	GEO: GSE181928
Experimental Models: Cell Lines		

Reagent or Resource	Source	Identifier
HCT116	ATCC	Cat#: CCL-247
Experimental Models: Organisms/Strains		
Mettl14(flox/flox) mice	Chuan He	Dev. Cell, 2020, 55(6): 737-753
Clu-CreERT2 mice	Alex Gregorieff	Nature, 2019, 569:121-125
B6.Cg-Tg(Vil1-cre)997Gum/J mice	Jackson Laboratory	Stock No: 004586
B6.Cg-Tg(CDX2-cre)101Erf/J mice	Jackson Laboratory	Stock No: 009350
B6.129P2-Lgr5$^{tm1(cre/ERT2)Cle}$/J mice	Jackson Laboratory	Stock No: 008875
B6.Cg-Tg(CDX2-Cre/ERT2)752Erf/J mice	Jackson Laboratory	Stock No: 022390
Hopx$^{tm2.1(cre/ERT2)Joe}$/J mice	Jackson Laboratory	Stock No: 017606
B6;129-*Bmi1*$^{tm1(cre/ERT)Mrc}$/J mice	Jackson Laboratory	Stock No: 010531
hGSDMC transgenic mice	This work	N/A
Oligonucleotides		
All oligonucleotide sequences are listed in Supplemental Table S2.		
Recombinant DNA		
pRP-CMV	VectorBuilder	N/A
pLV[Exp]-EGFP-EF1A>hGSDMC[NM_031415.3]	VectorBuilder	ID: VB201119-1182gke
pLV[shRNA]-EGFP-U6>hGSDMC-shRNA2	VectorBuilder	ID: VB201124-1144qsp
pLV-Neo-EF1A-hMETTL14	VectorBuilder	ID: VB191018-1246kgq
pLV-Neo-EF1A-GFP	VectorBuilder	N/A
Software and Algorithms		
ImageJ	NIH	https://imagej.nih.gov/ij/
Prism 8.4.2	GraphPad	https://graphpad-prism.software.informer.com
10x Genomics Cell Ranger 3.1.0	(Zheng et al., 2017)	https://support.10xgenomics.com/single-cell-gene-expression/software/overview/welcome
trim galore v0.6.5	RRID:SCR_011847	https://github.com/FelixKrueger/TrimGalore
STAR v2.6.1d	(Dobin et al., 2013)	https://github.com/alexdobin/STAR
Hisat2	(Kim et al., 2015)	http://www.ccb.jhu.edu/software/hisat/index.shtml
exomePeak	(Meng et al., 2013)	http://compgenomics.utsa.edu/exomePeak/
HOMER v4.10.0	(Heinz et al., 2010)	http://homer.ucsd.edu/homer/changeLog.html
Seurat v3	(Stuart, Butler, et al., 2019)	https://satijalab.org/seurat/articles/install.html
DoubletDecon	(DePasquale et al., 2019)	https://github.com/EDePasquale/DoubletDecon
R 4.0.2	(R Core Team, 2020)	https://www.r-project.org/
ChIPseeker	(Yu, Wang, and He 2015)	https://www.bioconductor.org/packages/release/bioc/html/ChIPseeker.html
clusterProfiler	(Yu et al., 2012)	http://bioconductor.org/packages/release/bioc/html/clusterProfiler.html
scRNA-seq analysis workflow	zenodo	https://doi.org/10.5281/zenodo.6653388